MRRT: Modeling of multiple reflections of radiation between terrains applied on the lunar surface region

Yunfei Liu [1,1]

[1]Shanghai Institute of technical physics

October 31, 2023

Abstract

The lunar surface has a stable luminosity. To use the Moon as a calibration standard, the Robotic Lunar Observatory (ROLO) program models the integration of the radiance of the entire lunar surface. However, the albedos of the mare and the highlands are very different. The modeling based on the lunar global irradiance/reflected radiance is bound to result in higher uncertainty. In contrast, if the local calibration of the lunar surface is adopted, the lunar complex topography effect cannot be ignored. This paper presents a new model for quantifying multiple reflections of radiation between terrains (MRRT). The relationship between the bidirectional reflectance factor (BRF) of the observed pixel and the true microtopography reflectance is established, which shows that the BRF is mainly influenced by the true topography reflectance, the terrain undulation, the incident irradiance on the topography surface, and the masking in the observation direction. The new model applied on the lunar surface obtains clearer terrain details. The inversion reflectance of the Chang'e-3 landing area is closer to the reflectance measured in situ, and the reflectance curves of the Apollo 16 landing area are almost consistent under different illumination observation geometries. This shows that the MRRT model can effectively eliminate the topographic effect. Compared with the ROLO model, the MRRT model does not restrict the specific selection, so it can select a region with a uniform material distribution, small albedo difference, and low topography undulation to establish the lunar surface radiometric calibration field with the advantage of providing stable radiation characteristics.

MRRT: Modeling of multiple reflections of radiation between terrains applied on the lunar surface region

Yunfei Liu, Qiang Guo and Guifu Wang

***Abstract*—The lunar surface has a stable luminosity. To use the Moon as a calibration standard, the Robotic Lunar Observatory (ROLO) program models the integration of the radiance of the entire lunar surface. However, the albedos of the mare and the highlands are very different. The modeling based on the lunar global irradiance/reflected radiance is bound to result in higher uncertainty. In contrast, if the local calibration of the lunar surface is adopted, the lunar complex topography effect cannot be ignored. This paper presents a new model for quantifying multiple reflections of radiation between terrains (MRRT). The relationship between the bidirectional reflectance factor (BRF) of the observed pixel and the true microtopography reflectance is established, which shows that the BRF is mainly influenced by the true topography reflectance, the terrain undulation, the incident irradiance on the topography surface, and the masking in the observation direction. The new model applied on the lunar surface obtains clearer terrain details. The inversion reflectance of the Chang'e-3 landing area is closer to the reflectance measured in situ, and the reflectance curves of the Apollo 16 landing area are almost consistent under different illumination observation geometries. This shows that the MRRT model can effectively eliminate the topographic effect. Compared with the ROLO model, the MRRT model does not restrict the specific selection, so it can select a region with a uniform material distribution, small albedo difference, and low topography undulation to establish the lunar surface radiometric calibration field with the advantage of providing stable radiation characteristics.**

***Index Terms*—Effect of microtopography inside remote sensing observation pixels, multiple-reflection-process modeling of radiation between terrains, and inversion of lunar surface reflectance**

I. Introduction

THE Moon is a nearby atmosphere-less body that reflects solar radiation [1]. For fixed illumination and fixed observation geometry, the Moon can be considered photometrically stable up to 10^{-8} per annum in irradiance [2]. Therefore, the Moon can serve as an ideal external calibration source for remote sensing instruments in the reflected solar band. The United States Geological Survey ran the Robotic Lunar Observatory (ROLO) ground-based observational program to establish an empirical lunar radiation model, which is based on observational data and modeling the integration of the radiance of the entire lunar surface at different times [3]. Although the ROLO model is currently the most accurate lunar radiation model worldwide, it still has an uncertainty of 5% to 10% [4]. One of the reasons is that the ROLO model reflectance is adjusted by using the laboratory reflectance of returned Apollo samples. The reflectance of returned Apollo soil samples in the laboratory is significantly different from that from lunar observations because of the difference in gravity between the Moon and Earth [5]. To improve the ROLO model, Zhang et al. [5] proposed using the mean equigonal albedo to replace the reflectance of Apollo soil samples; the new model's irradiance values in the visible and near-infrared (VNIR) bands are closer than those of the traditional ROLO model to the observations from the Moderate Resolution Imaging Spectroradiometer (MODIS) and Sea-viewing Wide Field-of-view Sensor (SeaWiFS). Sun et al. [6] developed a new model based on MODIS instrument observations to compensate for the shortcomings of the ROLO model in lunar irradiance measurement, which significantly improved the MODIS lunar calibration results of the entire mission. In fact, the Moon is not an ideal Lambertian body, and the albedos of different regions of the lunar surface are quite different (see Table I [7]). A modeling method based on the global irradiance/reflected radiance of the Moon is bound to result in higher uncertainty.

Large and small impact craters are densely distributed on the lunar surface [8]. At the meter to hectometer scales, there are obvious differences in the median bidirectional slope, root-mean-square (RMS) height, and median absolute slope between mares and highlands [9]. The details of the luminosity properties of the lunar surface are complicated by the macroscopic roughness of the Moon [10]. Rugged terrain often alters illumination and viewing geometry and generates a relief shadow, observation masking, and multiple scattering, which result in intense topographic dependence on the total incident reflectance or radiance [11]–[13]. According to different terrane types of the lunar surface, Wu et al. [14] divided the moon into four classes of albedo types and established a lunar irradiance model based on Chang'e-1 imaging interferometer (IIM) data; however, their model has some shortcomings in that the wavelength range is too narrow, and the model errors in high-latitude areas and border areas are relatively large. If a local area on the lunar surface is used for calibration, it is necessary to consider incorporating topographic data to study the problem of rim modeling and to improve the irradiance simulation accuracy [14].

At present, empirical models such as the Lommel-Seeliger model [15] and Sandmeier model [16] are often adopted for the calibration of lunar photometric observations. Alternatively, the Hapke radiative transfer model with simplified parameters or other models can be used [17]. Empirical models are often prone to overcorrection due to their simple parameters [18],

This work was supported by National Natural Science Foundation of China under Grant 41875037 and project for FY-4 ground-based visible and infrared lunar observation system of Shanghai Institute of Technical Physics, Chinese Academy of Sciences (No. O9KCE033N3). (Corresponding author: Qiang Guo.)

Manuscript received April 19, 2021; revised August 16, 2021

TABLE I
ALBEDO COMPARISON OF LUNAR SURFACE FEATURE REGIONS OBTAINED BY DIFFERENT OBSERVERS [7]

Feature areas on the lunar surface	Sytinskaya (1952)	Shorthill (1968)	Pohn (1966)
The darkest point	0.050	0.0516	0.070
The most bright spot	0.180	0.2190	0.240
Mare Crisium	0.062	0.0631-0.0784	0.085-0.096
Mare Foecunditatis	0.069	0.0655	0.090-0.108
Oceanus Procellarum	0.051-0.070	0.0533-0.0737	0.079-0.096
Sinus Iridum	0.065	0.0674	0.085-0.096
Mare Tranquillitatis	0.066	0.0571-0.0668	0.085-0.108
Mare Serenitatis	0.070	0.0585-0.0692	0.090-0.114
Mare Frigoris	0.089	0.0738	0.102-0.127
Mare Imbrium	0.054-0.074	0.0632	0.086-0.102
Mare Vaporum	0.060	0.0657	0.090-0.108
Mare Nubium	0.062-0.073	0.0627-0.0705	0.090-0.108
Tycho	0.154	0.0742 -0.1737	0.150-0.169

[19], but the Hakpe model [20]–[23] is difficult to apply due to its numerous parameters, mathematical coupling, and high requirements regarding observation data [17]. With the improvement of computing power, 3D computer simulation models play an increasingly important role in the study of the radiation characteristics of complex surfaces [24]. The main principles of computer modeling include ray tracing and radiosity methods. Using statistical analysis by computers, the distribution of lunar soil particles can be simulated. Muinonen et al. [25] used the Monte Carlo ray tracing method to analyze the single-scattering albedos and phase functions, local surface roughness, and regolith porosity of specific lunar mare regions imaged by the Advanced Moon micro-Imager Experiment (AMIE) camera onboard the ESA SMART-1 mission. Wong et al. [26] combined Monte Carlo ray tracing and Hapke models to model reflectance considering both (surface) large scale and (interparticle) microscale effects. However, Wong used a typical simple illumination model, the Phong model, which does not consider reflection between terrain surfaces.

In ground remote sensing detection, Pory et al. [27] assumed that the surface is Lambertian and proposed that the radiation received by a surface consists of direct solar radiation, scattered atmospheric radiation, and adjacent terrain-reflected radiation. The reflected radiation from the surrounding terrain is defined as the sum of the solar radiation reflected on the target pixel by other visible pixels (see Equation (4)). Nevertheless, the calculation of reflected radiation from the surrounding terrain only considers the first-order scattering effect between terrains. The attenuation of the signal between two adjacent slopes and second-order reflection are neglected [27]. In remote sensing on Earth, the multiple reflections of radiation between terrains are often attenuated greatly due to the influence of air, but for the lunar surface with atmosphereless, the multiple reflections of radiation between terrains should be given more attention.

In this paper, a new model for quantifying multiple reflections of radiation between terrains (MRRT) is presented. Based on the adjacent terrain irradiance formula of the first-order reflection proposed by Proy, the second-order to the nth-order reflections of radiation between terrains are derived. Moreover, the relationship between the bidirectional reflectance factor (BRF) of the observed pixel and the true microtopography reflectance is established, which shows that the BRF is mainly influenced by the true topography reflectance, the terrain undulation, the incident irradiance on the topography surface, and the masking in the observation direction.

In Section II, the modeling process of multiple reflections of radiation between terrains is described in detail. In Section III, the experimental area and data selected in this paper are introduced. In Section IV, we apply the new model to the experimental area and compare it with the dataset to discuss its results. Finally, in Section V, we summarize the content of this paper and prospect the application scenarios of the new model.

II. THEORY

Direct solar radiation over rugged terrain is the most important component of the total incident radiation that illustrates the surface [13]. In addition, the adjacent terrain-reflected irradiance increases the total radiation reaching the slope surface [27]. As shown in Fig. 1, M and P are mutually visible. When point P has a reflected radiance greater than zero, point M must be reflected by point P; that is, M receives both incident radiation from the sun and radiation reflected from point P. Obviously, for the lunar surface with almost no atmospheric attenuation, the reflection of radiation between terrains (such as points P and M) is performed multiple times.

Assuming that the total solar incident radiation flux of the target terrain is Φ_{sun} (limited area size and no other incident radiation source), the total radiation flux of the first reflection is Φ_1, and after k reflections, the total radiation flux is Φ_k. The relationship among Φ_{sun}, Φ_1 and Φ_k can be expressed by the following formula:

$$\Phi_{sun} > \Phi_1 > \Phi_2 > \cdots > \Phi_k \tag{1}$$

and

$$\Phi_{sun} > \Phi_1 + \Phi_2 + \cdots + \Phi_k \tag{2}$$

where Φ_k infinitely approaches zero.

The target terrain is divided into equal space intervals so that multiple microareas with different slope, aspect, and elevation values are formed. This has the advantage of simplifying the shape of the terrain to discuss how the radiation varies from

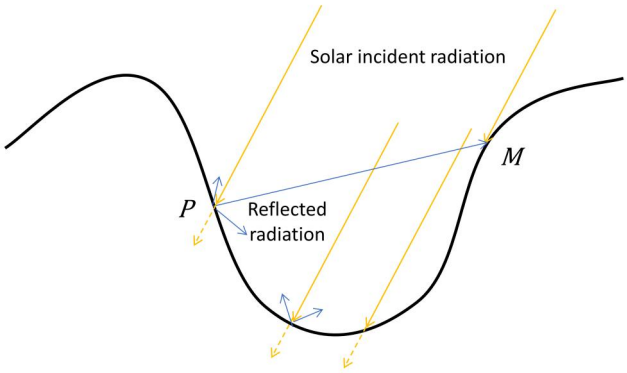

Fig. 1. Slope P reflects radiation to slope M, and P adds a source of irradiation for M. The solid yellow line is the solar incident radiation; the yellow dashed line is the absorbed solar radiation; and the solid blue line is the radiation reflected by the terrain.

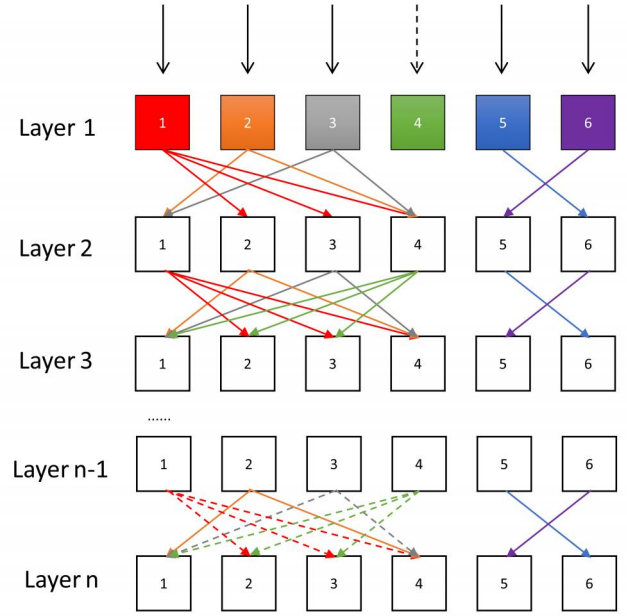

Fig. 2. Schematic representation of an "update" of a radiative source for a microarea. The dashed lines represent that there is no incident radiation, and the solid lines indicate that there is incident radiation. Arrows of different colors represent the reflected radiation from different microareas, in which the microareas indicated by arrows represent a mutually visible. In contrast, the microareas with no arrows indicate that there is no visible. The first layer receives the solar incident radiation, and the second to nth layers receive the reflected radiation from other slopes in the previous layer.

microarea to microarea. As shown in Fig. 2, every reflection of radiation between terrains will cause changes in incident radiation on the surface of microareas. We call this change in incident radiation on the surface of the microarea an "update" of incident radiation on the microarea surface.

A. Updating the incident radiation on the surface of a microarea

1) One-time reflection between terrains: The surfaces with different reflectance are assumed to be Lambertian. As shown in Fig. 1, the radiance received by point M from point P can be written as [27]:

$$L_{(P\to M)} = \frac{L_P \cdot dS_M cosT_M \cdot dS_P cosT_P}{r_{MP}^2} \tag{3}$$

where dS_M and dS_P are the areas of pixels M and P, respectively; T_M and T_P are the angles between the normal to the ground and the line MP; L_P is the luminance of P; and r_{MP} is the distance between M and P. If ρ_P is the reflectance of pixel P illuminated by the irradiance E_P, then $L_P = \rho_P E_P/\pi$. The subscript $P \to M$ represents the transfer of radiation from P to slope M.

Therefore, the total irradiance received by slope M from all "visible" P [27] can be written as:

$$E_M = \sum_j \frac{L_{(P_j\to M)}}{dS_M} = \sum_j \rho_{P_j} \frac{E_{P_j} cosT_M cosT_{P_j} dS_{P_j}}{\pi r_{MP_j}^2} \tag{4}$$

2) Multiple reflections between terrains: As noted in the previous section, if $\rho_M \Phi_M$ is not 0 (where ρ_M is the reflectance of M and Φ_M is the total incident radiation flux received by the slope M from other visible slopes after one-time reflection), then $\rho\Phi_M$ will continue to participate in the next reflection with other slopes. Therefore, the incident irradiance on each microarea surface after each radiation reflection can be obtained as follows:

$$E_M(1) = E_{(sun\to M)}, \qquad E_{P_j}(1) = E_{(sun\to P_j)} \tag{5a}$$

$$E_M(n) = \sum_j \rho_{P_j} \frac{cosT_M cosT_{P_j} dS_{P_j}}{\pi r_{MP_j}^2} \cdot E_{P_j}(n-1) \tag{5b}$$

where $E_M(n)$ represents the total incident irradiance received by the slope M surface for the nth time.

Let

$$\Gamma_{MP_j} = \frac{cosT_M cosT_{P_j} dS_{P_j}}{\pi r_{MP_j}^2} \tag{6}$$

where Γ_{MP_j} can be considered the visible radiation factor between P_j and M. Obviously, Γ_{MP_j} does not vary with the number of reflections. Equation (5b) can be simplified as:

$$E_M(n) = \sum_j \rho_{P_j} \Gamma_{MP_j} \cdot E_{P_j}(n-1) \tag{7}$$

Then, after the multireflection between terrains, the total reflected radiance $L_{M_{ref}}$ of slope M to the sky can be expressed as:

$$L_{M_{ref}} = \frac{\rho_M}{\pi}[E_M(1) + E_M(2) + \cdots + E_M(n)] \tag{8}$$

Equation (8) shows that the solar direct incident irradiance on the slope surface, the mutual visibility between slopes and the reflectivity of slopes directly affect the multiple reflection process and results.

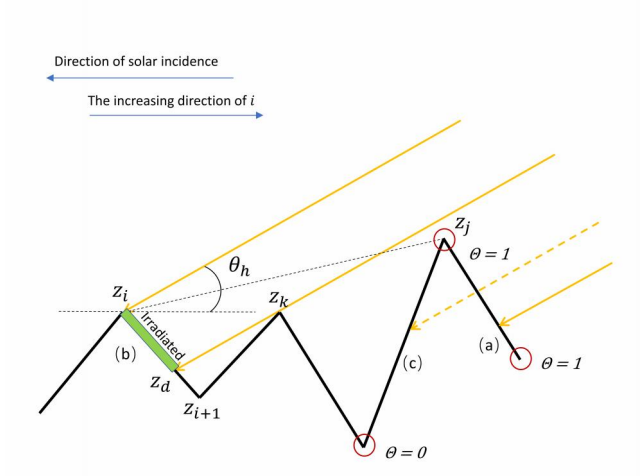

Fig. 3. There are three types of cases in which any slope receives solar radiation: (a) fully irradiated, (b) partially irradiated, and (c) no irradiation. θ_h is the solar altitude angle.

B. Direct solar incident irradiance on microtopography surfaces

Changes in altitude affect the distribution of solar radiation, resulting in sunlit and shaded areas that correspond to bright and dark pixels in remote sensing images [28]. In general, on slopes of rugged terrain, the most important variable controlling incident radiation is the local solar illumination angle [29]. If the sun is not hidden by a local horizon, the local illumination angle θ_s on a slope S with azimuth A is given by:

$$cos\theta_s = cos\theta_0 cosS + sin\theta_0 sinScos(\phi_0 - A) \tag{9}$$

where θ_0 is the illumination angle on a horizontal surface and ϕ_0 is the azimuth of illumination.

Shadows refer to regions lacking direct solar illumination, which can be attributed to two reasons: opposing the sun and cast by obstructions [30]. As shown in Fig. 3, for any slope, the received solar irradiation can be divided into three types: (i) fully irradiated, (ii) partially irradiated, and (iii) no irradiation. First, it is determined whether the two ends of a slope can be irradiated, and the result is used to establish the actual irradiated condition of the slope.

1) Incident irradiance of a one-dimensional terrain surface: We form grid points with elevation values. For a grid row, an elevation function z is defined for the points $j = 0, 1, \ldots, N-1$. Since the points are evenly spaced, the abscissa is specified by $j\Delta h$ [29]. A binary factor Θ is established to indicate whether elevation point z_j is irradiated. When $\Theta = 1$, z_j is irradiated; when $\Theta = 0$, z_j is not irradiated (see Fig. 3).

Therefore, for all $0 \leq i < N$, when the direction of solar incidence is the opposite of the increasing direction of i: for all $i < j < N$, if

$$max(\frac{z_j - z_i}{j - i}) > tan(\theta_h) \tag{10}$$

where θ_h is the solar elevation angle. There is at least one point $j < N$ that can be connected to i to form a new slope so that the elevation angle of the new slope is greater than that of the sun. This indicates that point i cannot be irradiated; thus, $\Theta_i = 0$. Otherwise, $\Theta_i = 1$.

For all $0 \leq i < i+1 < N$, let dS_i denote the slope consisting of the ith and the $(i+1)$th elevation values. If $\Theta_i = 0$, dS_i is not irradiated at all; if $\Theta_i = 1$ and $\Theta_{i+1} = 1$, dS_i is fully irradiated. Then, the irradiance formula can be expressed as:

$$E_i = E_{sun}\cos(\vec{N}, \vec{S}), \qquad when\ \Theta_i = 1,\ \Theta_{i+1} = 1 \tag{11}$$

$$E_i = 0, \qquad when\ \Theta_i = 0 \tag{12}$$

If $\Theta_i = 1, \Theta_{i+1} = 0$, then dS_i is partially irradiated, as shown in Fig. 3. The size of the irradiated area depends on the maximum occlusion point corresponding to z_{i+1} (denoted as z_k). The critical point at which the slope dS_i receives solar radiation can be obtained from the intersection of the line and $z_i z_{i+1}$ of solar rays passing through the point z_k. Assuming that the critical point is z_d, the irradiance formula for this irradiated area is:

$$E_i = \frac{|z_i\vec{z}_d|}{|z_i\vec{z}_{i+1}|}E_{sun}\cos(\vec{N}, \vec{S}), \qquad when\ \Theta_i = 1, \Theta_{i+1} = 0 \tag{13}$$

where E_{sun} is the direct solar irradiance, $\vec{N}$ is the normal to the terrain and $\vec{S}$ is the solar angle.

2) Incident irradiance of a two-dimensional terrain surface: The topographic effects on solar irradiance are mainly variations in illumination angle and shadowing from local horizons [29]. Due to the irregular nature of the ground in rugged areas, the sky dome overlying a surface is not the integrated hemisphere of a horizontal surface [31]. Dozier [32] proposed determining the local horizon information from a grid. At any location, the portion of the overlying hemisphere that is obscured by terrain is:

$$\frac{1}{2\pi}\int_0^{2\pi} sin(h[\theta])d\theta \tag{14}$$

where $h[\theta]$ is the horizon angle in the direction θ. These horizons, however, are difficult to compute because, unlike slope and azimuth, they cannot be generated from information restricted to the immediate neighborhood of a point.

By rotating a grid in direction ϕ_0, we reduce the horizon problem to its one-dimensional equivalent. Our interest is the angle to the horizon from any point in any direction, but we formulate the problem by determining the coordinates of the points that form the horizons. Minor errors in the elevation grid can therefore shift the "answer", i.e., the coordinates of the horizon point, by a considerable distance, but minor errors do not cause much variation in the end result, which is the angle to the horizon. When available digital terrain grids are sufficiently smooth, interpolation does not change the results [32]. In Appendix A, we discuss the effect of different interpolation methods on the error caused by image rotation.

A suitable interpolation method is selected for the rotation of the grid so that the relative azimuth of the incident solar

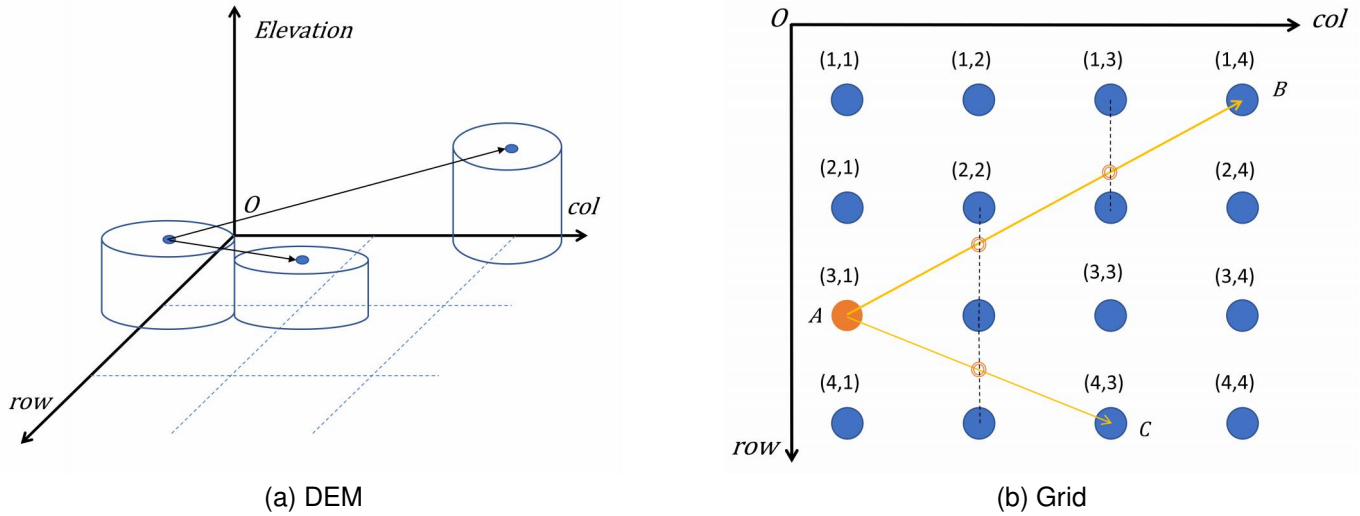

Fig. 4. The mutual reflection between microarea surfaces is reduced to the mutual visibility between grid points. One grid point represents a flat cylinder whose height is the elevation value of the terrain. In (b), A is the radiation source, and B and C are the target receiving points; the yellow line is the radiation emitted by A; and the double circles are the actual elevation positions on the radiation path.

ray is $0°$. In this paper, the bicubic interpolation method with the minimum error after the two times rotation is used. The kernel function of bicubic interpolation [33] is as follows:

$$u(s) = \begin{cases} (a+2)|s|^3 - (a+3)|s|^2 + 1, & 0 < |s| < 1 \\ a|s|^3 - 5a|s|^2 + 8a|s| - 4a, & 1 < |s| < 2 \\ 0, & 2 < |s| \end{cases} \tag{15}$$

where a is equal to -0.5.

The rotated grid is calculated using the one-dimensional terrain surface incident irradiance method, and then the calculated matrix is rotated in the inverse direction of ϕ_0 to obtain the irradiance of the original grid.

It is assumed that the final solar direct incident irradiance is represented by matrix E_0, which can be written as:

$$E_0 = \begin{bmatrix} E_{11} & E_{12} & \cdots & E_{1c} \\ E_{21} & E_{22} & \cdots & E_{2c} \\ \vdots & \vdots & \ddots & \vdots \\ E_{r1} & E_{r2} & \cdots & E_{rc} \end{bmatrix} \tag{16}$$

E_{rc} represents the actual solar incident irradiance received by the grid points located in row r and column c.

C. Visible radiation factor between terrains

To quantify the magnitude of the new incident radiation on the surface of a microarea after each reflection, we need to determine in advance what other surfaces can reflect the target. In this paper, the mutual reflection between surfaces is reduced to the mutual visibility between grid points. One grid point represents a flat cylinder whose height is the elevation value of the terrain, as shown in Fig. 4.

For a given terrain, the mutual reflection relationship between any slope pair is also certain. We first calculate whether there is a reflection between any two slopes; the calculation result can be stored in advance so that it can be called directly

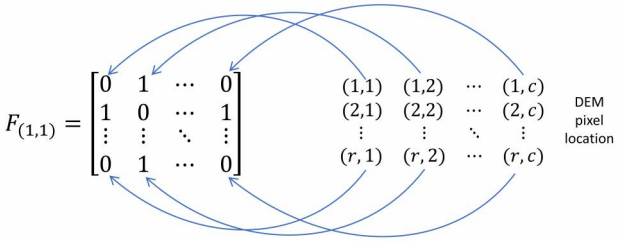

Fig. 5. Schematic diagram of the stored elements in the $F_{(1,1)}$ matrix corresponding to the position of the image.

in the later operation. The binary matrix $F_{(r,c)}$ stores the reflection relations between the grid point at position (r, c) and all other slope points, and the matrix elements are 0 or 1. As shown in Fig. 5, $F_{(1,1)}$ is used as an example: when $F_{(1,1)}(1,1) = 0$, the DEM pixel at position $(1,1)$ in the grid matrix includes no self-reflection; when $F_{(1,1)}(1,2) = 1$, reflection occurs between DEM pixels at position $(1,2)$ and pixels at position $(1,1)$.

We fit the elevation value of the "position" on the linear path between the "radiation source point" and the "target receiving point" by the adjacent point values and determine whether the radiation rays are "blocked". As shown in Fig. 4(b), there are not always true elevation points on the radiating paths of $A \to B$ and $A \to C$ (i.e., there are no elevation points at the double circle). We define the position of the elevation value passing on the radiation path between the radiation source and the target receiving point as the "intermediate slope point", which may or may not be present in the DEM. The number of intermediate slope points depends on the maximum distance between the radiation source and the target receiver in the row and col directions.

As shown in Fig. 6, the $Oxyz$ spatial Cartesian coordinate system is established, where x and y correspond to the row

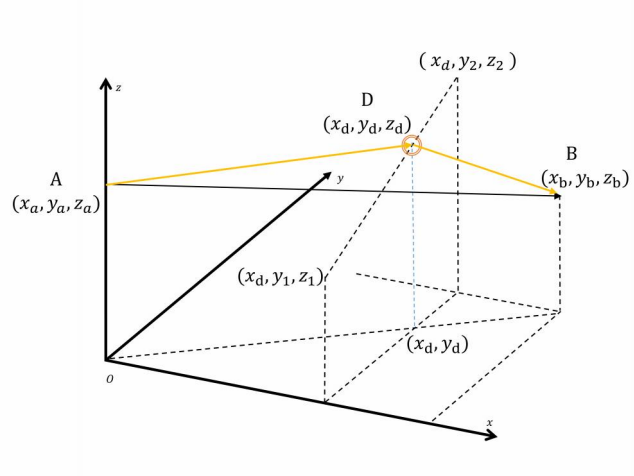

Fig. 6. Schematic diagram of the actual position and elevation of the intermediate slope point.

value and column value of the DEM image, respectively, and the unit interval is set to be equal to the spatial resolution of the DEM, denoted as t. The size of z is the ratio of the elevation value to the spatial resolution. Therefore, the units of x, y, and z are unified, i.e., $(t \cdot m/pixel)$. For any two points $A(x_a, y_a, z_a)$ and $B(x_b, y_b, z_b)$ in $Oxyz$,

(i) For $max(|x_a - x_b|, |y_a - y_b|) = 1$, the number of intermediate slope points is $num = 0$; that is, points A and B are adjacent, AB forms a slope, and there is no reflection for AB.

(ii) For $max(|x_a - x_b|, |y_a - y_b|) > 1$, if $|x_a - x_b| > |y_a - y_b|$, the number of intermediate slope points is $num = |x_a - x_b| - 1$. Let the intermediate slope point be $D(x_d, y_d, z_d)$. For $x_a < x_d < x_b$, y_d is the intersection of the perpendicular of $(x_d, 0)$ in the direction of y and the projection of AB in the two-dimensional plane of Oxy. $y1 = floor(y_d)$, and $y2 = ceil(y_d)$, where $z1$ is the elevation value of $(x_d, y1)$ and $z2$ is the elevation value of $(x_d, y2)$. Then, the formula for z_d is:

$$z_d = z_1 + \frac{y_d - y_1}{y2 - y1}(z_2 - z_1) \tag{17}$$

(iii) For $max(|x_a - x_b|, |y_a - y_b|) > 1$, if $|x_a - x_b| < |y_a - y_b|$, the number of intermediate slope points is $num = |y_a - y_b| - 1$. Let the intermediate slope point be $D(x_d, y_d, z_d)$. For $y_a < y_d < y_b$, x_d is the intersection of the perpendicular of $(0, y_d)$ in the direction of x and the projection of AB in the two-dimensional plane of Oxy. $x1 = floot(x_d)$, and $x2 = ceil(x_d)$, where $z1$ is the elevation value of (x_1, y_d) and $z2$ is the elevation value of $(x2, y_d)$. Then, the formula for z_d is:

$$z_d = z_1 + \frac{x_d - x_1}{x2 - x1}(z_2 - z_1) \tag{18}$$

Therefore, it is possible to calculate whether any point D on the "radiation path" of AB occludes AB. The judgment process is similar to that expressed in Equation (10). Alternatively, this judgement can be based on the position of z_d (i.e., whether z_d is above or below line AB).

Based on the binary matrix F of each pixel position, the visible radiation factor Γ of terrain corresponding to each pixel position can be obtained by combining Equation (6).

D. Matrix representation of multiple reflections between terrains

According to the content in the previous three sections, the multiple-reflection process between terrains is expressed in the form of a matrix. The microarea reflectance is assumed to be ρ, and Lambert reflection is considered. Let the matrix T_n store the incident irradiance on the surface of each DEM pixel of the nth-order, as shown in Equations (19) and (20):

$$T_1 = E_0 = \begin{bmatrix} E_{11} & E_{12} & \cdots & E_{1c} \\ E_{21} & E_{22} & \cdots & E_{2c} \\ \vdots & \vdots & \ddots & \vdots \\ E_{r1} & E_{r2} & \cdots & E_{rc} \end{bmatrix}, \qquad n = 1 \tag{19}$$

$$T_n = \rho^{n-1} \cdot \begin{bmatrix} sum(T_{n-1} \odot \Gamma_{(1,1)}) & sum(T_{n-1} \odot \Gamma_{(1,2)}) & \cdots & sum(T_{n-1} \odot \Gamma_{(1,c)}) \\ sum(T_{n-1} \odot \Gamma_{(2,1)}) & sum(T_{n-1} \odot \Gamma_{(2,2)}) & \cdots & sum(T_{n-1} \odot \Gamma_{(2,c)}) \\ \vdots & \vdots & \ddots & \vdots \\ sum(T_{n-1} \odot \Gamma_{(r,1)}) & sum(T_{n-1} \odot \Gamma_{(r,2)}) & \cdots & sum(T_{n-1} \odot \Gamma_{(r,c)}) \end{bmatrix}, \qquad n > 1 \tag{20}$$

$T_{n-1} \odot \Gamma_{(r,c)}$ represents the multiplication of each element in the corresponding position of matrix T_{n-1} and matrix $\Gamma(r, c)$, resulting in a matrix of the same size. $sum(T_{n-1} \odot \Gamma_{(r,c)})$ denotes adding all the elements of the resulting matrix. Each element in T_n gradually tends to 0 over multiple radiative reflections. Then, the final total reflected radiance of the whole DEM image to the sky L_{ref} can be expressed as:

$$L_{ref} = \frac{\rho}{\pi}(T_1 + T_2 + \cdots + T_n) \tag{21}$$

E. The total reflected radiance in the observed direction

Assume that the illumination of each microarea at the incident angle is given by matrix B_s and that the visibility of each microarea at the observation angle is given by matrix B_v. According to the principle of reciprocity of angles, $B_s = B_v$ at the same angle.

Therefore, let the incident radiation from the observation direction irradiance be 1 W/m^2. According to the aforementioned calculation method of actual incident irradiance on the surface, if in the observation direction the irradiance on the surface is greater than zero, then the surface can be "observed".

These areas are set to 1 in the matrix B_v, and the others are set to 0. Then, the binary visibility matrix B_v is obtained, such as:

$$B_v = \begin{bmatrix} b_{11} & b_{12} & \cdots & b_{1c} \\ b_{21} & b_{22} & \cdots & b_{2c} \\ \vdots & \vdots & \ddots & \vdots \\ b_{r1} & b_{r2} & \cdots & b_{rc} \end{bmatrix} \tag{22}$$

where $b_{rc} = 0$ or $b_{rc} = 1$. The binary matrix B_v represents the masking of the terrain in the observation direction.

Then, the reflected radiance L_v in a specific observation direction can be expressed as:

$$L_v = L_{ref} \odot B_v \tag{23}$$

F. The directional-directional reflectance factor of the area observed by the remote sensing pixel

Limited by the spatial resolution of remote sensing instruments, it is often difficult to obtain objects with uniform radiation characteristics at the pixel scale. The effect of topography on reflectance is usually concentrated on the comprehensive effect of the microslope in a remote sensing pixel. If we obtain high spatial resolution DEM data of the area corresponding to the pixel, the MRRT model can be used to obtain the directional-directional reflectance factor (BRF) (see Appendix B) of the area observed by the pixel.

Therefore, considering the effect of microtopography in a single remote-sensing observation pixel, the reflectance of microtopography is assumed to be ρ, and Lambert reflection is considered. Let $T_n = \rho^{n-1} \cdot D_{n-1}, (n > 2)$. D_{n-1} represents the $(n-1)$th reflection effect between terrains. When $n = 1$, $D_0 = T_1 = E_0$. L_{ref} can be expressed as:

$$L_{ref} = \frac{\rho}{\pi}(T_1 + T_2 + \cdots + T_n) = \frac{\rho D_0 + \rho^2 D_1 + \cdots + \rho^n D_{n-1}}{\pi} \tag{24}$$

Then, the BRF of the observation area of a single pixel is shown in Equation (25):

$$BRF(\theta_0, \phi_0, \theta_v, \varphi_v) = \frac{\pi L_v(\theta_0, \phi_0, \theta_v, \varphi_v)}{E_{sun} cos(\theta_0)} = \frac{\rho D_0 + \rho^2 D_1 + \cdots + \rho^n D_{n-1}}{E_{sun} cos(\theta_0)} \odot B_v \tag{25}$$

where θ_0, ϕ_0, θ_v, and φ_v are the solar zenith angle, solar azimuth angle, observation zenith angle, and observation azimuth angle, respectively. E_{sun} is the direct solar irradiance. When the topography is completely horizontally flat, there is only one reflection from the terrain surface. Therefore, $D_0 = E_{sun} cos(\theta_0)$, $B_v = 1$, and $BRF = \rho_v$.

Equation (25) establishes the relationship between the BRF of the observed pixel and the true reflectance of the microterrain inside the observed pixel area, which shows that the terrain effect on the BRF mainly comes from the true reflectance of the terrain surface, the terrain undulation, the incident irradiance on the terrain surface and the masking in the observation direction.

III. DATA

A. LOLA SLDEM

The Lunar Orbiter Laser Altimeter (LOLA) [34] is an instrument on the Lunar Reconnaissance Orbiter (LRO) spacecraft designed to acquire high-precision topographic data on the lunar surface [35]. Barker et al. [36] combined the DEMs obtained from the LOLA DEMs and SELENE terrain camera (TC) to produce a near-global DEM with higher geodetic accuracy, namely, SLDEM2015. SLDEM2015 can be found at http://imbrium.mit.edu/DATA/SLDEM2015/. This dataset is used in this paper, and the spatial resolution of the data is 512 pixels per degree with approximately 60 m per pixel. The obvious vertical stripes obtained by visual observation of LOLA SLDEM are preprocessed by replacing the stripes themselves with the mean values of the left and right columns of the stripes. As shown in Fig. 7, the processed image is visually transitional.

B. In situ measurements from the Chang'e-3 landing site and Apollo 16 lunar soil sample 62231

The Chang'e-3 landing site is located at 44.1205°N, 19.5102°W [37], and a large area around the landing site has a homogeneous composition. Compared to the MS-2, Apollo 15, and Apollo 16 highland sites, the CE-3 site is much younger and less impacted and contaminated [38]. Therefore, the Chang'e-3 landing site and its in situ spectra are proposed as an optical standard for both radiance calibration and wavelength calibration for lunar and Earth-orbital missions [38].

The Visible-Near Infrared Spectrometer (VNIS) instrument onboard the Yutu probe made measurements at four different points (E, S3, N203, and 205, as shown in Fig. 8) and obtained data in detection mode four times and calibration mode three times. All these data are available at https://moon.bao.ac.cn/.

Apollo 16 is located at approximately 15.5°E, 9°S, on the relatively flat Cayley Plain, adjacent to the rugged Cartesian crater. Apollo 16 collected rock samples from the highlands, and, after that, some sample parameters were measured by the Lunar Soil Characterization Consortium (LSCC) laboratory. Therefore, the area near the Apollo 16 lunar landing site is generally selected as the research area to invert the reflectance, albedo, and mineral content of the lunar surface. Apollo 16 lunar soil sample 62231 is a typical representative of this landing site, which is characterized by high maturity and stable spectral properties [1].

The reflectance factor (REFF) spectra [38] for the CE-3 in situ measurements and the bidirectional reflectance spectra [1] of lunar soil sample 62231 are shown in Fig. 9.

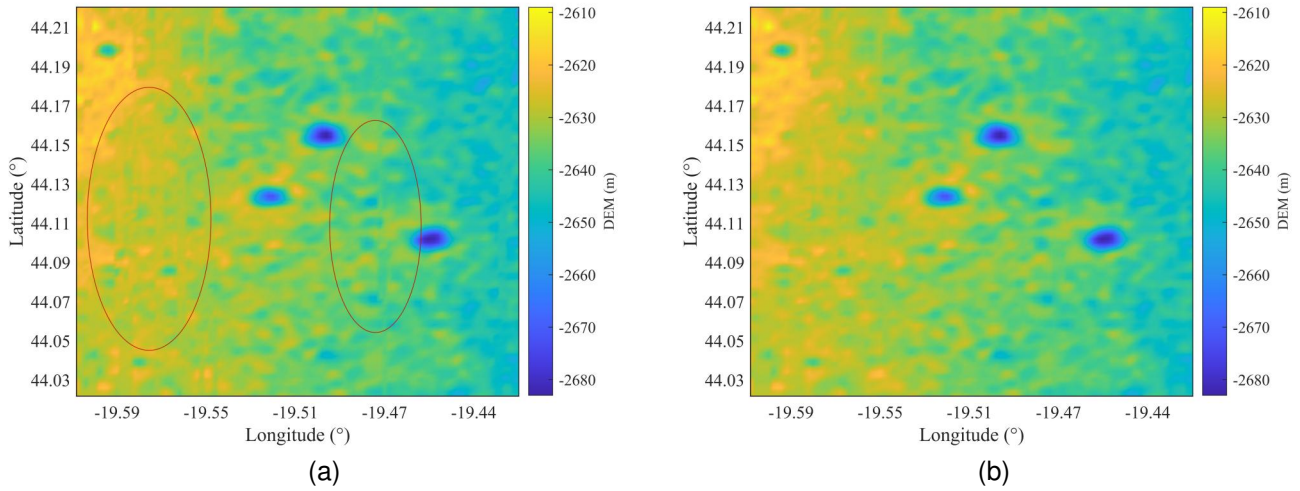

Fig. 7. DEM area display and image preprocessing results. (a) The original image; (b) the processed image.

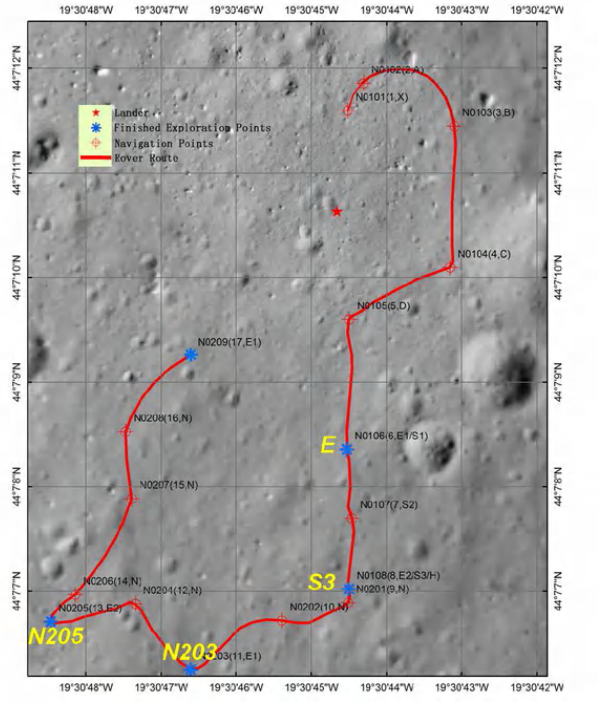

Fig. 8. Map of the path traversed by the Yutu rover and the distribution of detection points [39]

C. IIM orbit data

The interference imaging spectroradiometer (IIM) onboard Chang'e-1 achieved 84% coverage of the lunar surface between 70°S and 70°N using push-broom hyperspectral imaging, with a spatial resolution of 200 m per pixel. The IIM achieves 32-band multispectral observations over the spectral range 480-960 nm [40]. The first five bands (480-513 nm) and the last band (946 nm) of the IIM are abnormal and should be eliminated before use [38].

In this study, the data we used are CE-1 IIM 2B radiance data. The solar irradiance J at the surface of the IIM was calculated using Equation (26) based on the known spectral curve of the solar irradiance of the surface and the corresponding spectral response function of the IIM [17]. The solar irradiance E_{sun} is taken from the New Synthetic Gueymard Spectra [41] because it is used by the CE-3 team for the onboard calibration of the VNIS [38].

$$J = \frac{\int_{\lambda_1}^{\lambda_2} E_{sun}(\lambda) f(\lambda,\sigma) d\lambda}{\int_{\lambda_1}^{\lambda_2} f(\lambda,\sigma) d\lambda} \tag{26}$$

Here, $f(\lambda,\sigma)$ is the corresponding spectral response function of the IIM, and λ_1 and λ_2 are the start and end wavelengths of $f(\lambda,\sigma)$, respectively. The spectral response function of the IIM can be simulated with the central wavelength and full width at half maximum (FWHM) as follows [17]:

$$f(\lambda,\sigma) = \exp\left[-\frac{(\lambda-\lambda_c)^2}{2\sigma^2}\right] \tag{27}$$

In Equation (27), $\sigma = \frac{FWHM}{2\sqrt{2\ln 2}}$, and λ_c is the center wavelength.

IV. Results

A. Comparative analysis of radiance for a single reflection and multiple reflections

Six regions are selected on the lunar surface (see Fig. 10). The topographic data are obtained from the LOLA SLDEM with a spatial resolution of approximately 60 m. The solar zenith angle, solar azimuth angle, observation zenith angle, observation azimuth angle, and solar incident irradiance are assumed to be 30°, 0°, 0°, 0°, and 100 W/m^2, respectively. When the microarea reflectances are $\rho = 0.03$, $\rho = 0.15$, and $\rho = 0.3$, calculations are performed for a single reflection (i.e., the adjacent terrain irradiance calculation term of the Proy model) and multiple reflections (i.e., the MRRT model in this paper).

Figs. 11, 12, 13, 14, 15 and 16 show that the radiance transition of adjacent positions in the images with a single

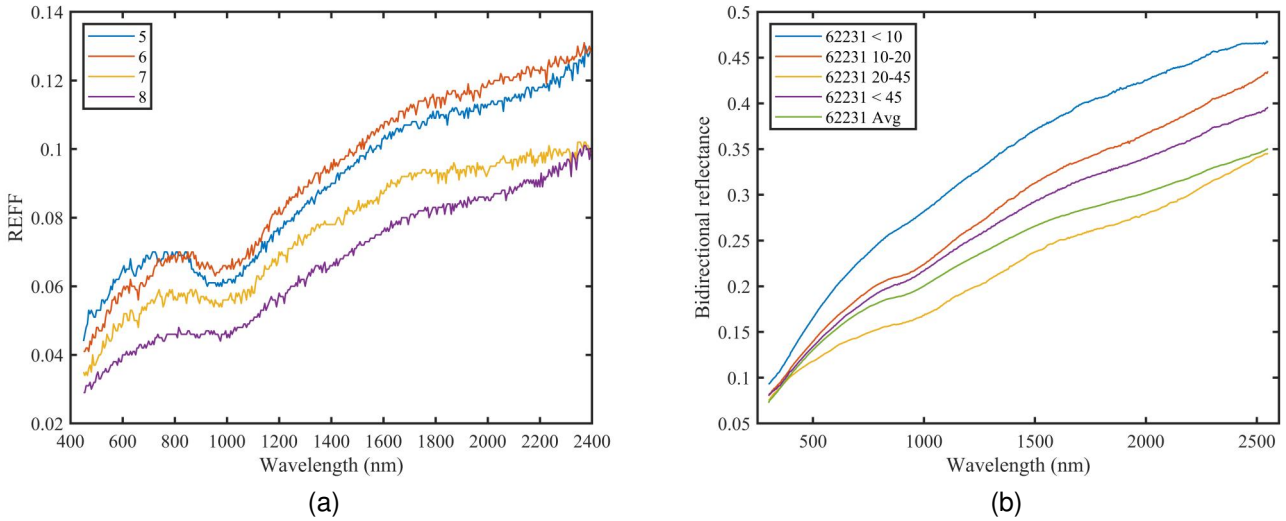

Fig. 9. Reflectance spectra. (a) In situ REFF for the VNIS measurements and (b) bidirectional reflectance spectra of lunar soil sample 62231.

reflection is very abrupt, while that in the images with multiple reflections is gentle. Compared with the radiance result of a single reflection, the result of multiple reflections is more consistent with the real reflected radiance of the terrain, and more topographic details are shown. Moreover, the radiance with multiple reflections is larger than the radiance with a single reflection because the irradiance on the microtopography surface is increased by the multiple reflections between terrains. When the microtopography reflectance is small, the increase in radiance is not obvious, but as the reflectance increases, the increase in radiance is larger. This indicates that the effect of multiple reflections of radiation between terrains is nonnegligible on the lunar surface regions.

In addition, subfigures (e) and (f) in these figures all show some stripes, which are not eliminated when preprocessing the image because it is difficult to find them visually in the SLDEM image. From another view, the results show that the topography information is not broken when the calculation of the MRRT is performed, that is, the MRRT is reliable. Furthermore, the new model more easily verifies the reliability of the original data from the results than the one reflection irradiance formula, so the preprocessing of the original data can be checked again.

B. Effect of microtopography on the directional-directional reflectance of the target area

The solar zenith angle, solar azimuth angle, observation zenith angle, observation azimuth angle, and solar incident irradiance are assumed to be 30°, 0°, 0°, 0°, and 100 W/m^2, respectively. The percentage increase in the BRF (see Equation (B2)) of the target regions relative to the microarea reflectance ρ is calculated.

Fig. 17 shows that for the same area, the difference between the BRF of the target region and the true reflectance of microtopography increases significantly with the increase in the reflectance of the microtopography. This is because the increase in microtopography reflectance will lead to an increase in multiple reflections between terrains, thus increasing the incident irradiance of the microtopography surface and the reflected radiance in the observation direction. According to Equation (25), the value of the denominator remains the same, and the numerator L_v increases with the increase in the number of reflections between terrains, so the BRF increases.

For the same microtopography reflectance, the BRFs of different areas with the same illumination observation geometry also have obvious differences, and the differences increase significantly with the increase in microtopography reflectance.

C. Inversion of microtopography reflectance with the same illumination observation geometry

The solar zenith angle, solar azimuth angle, observation zenith angle, and observation azimuth angle are assumed to be 30°, 0°, 0°, and 0°, respectively. When the solar incident irradiances are 1, 10, and 100 W/m^2, the reflected radiance of a completely flat region, assuming its microtopography reflectance is 0.15, can be obtained, i.e., 0.0413, 0.4135, and 4.1350 $W/m^2/sr$, respectively. The calculation formula is as follows (let the flat region be Lambertian):

$$L_{flat} = \rho_{flat} \frac{E_{flat} cos(\theta_0)}{\pi} \tag{28}$$

where E_{flat}, ρ_{flat}, and L_{flat} are the direct solar irradiance, the microtopography reflectance of the flat region, and the reflected radiance of the flat region, respectively. θ_0 is the solar zenith angle.

Let the reflected radiance of the flat region be the observed radiance, then the microtopography reflectances of the six regions are retrieved.

Table II shows that the inversion reflectance of the microtopography of the six regions is less than 0.15 (i.e., less than the microtopography reflectance of the flat area). Solar irradiance has little effect on the inversion results of microtopography

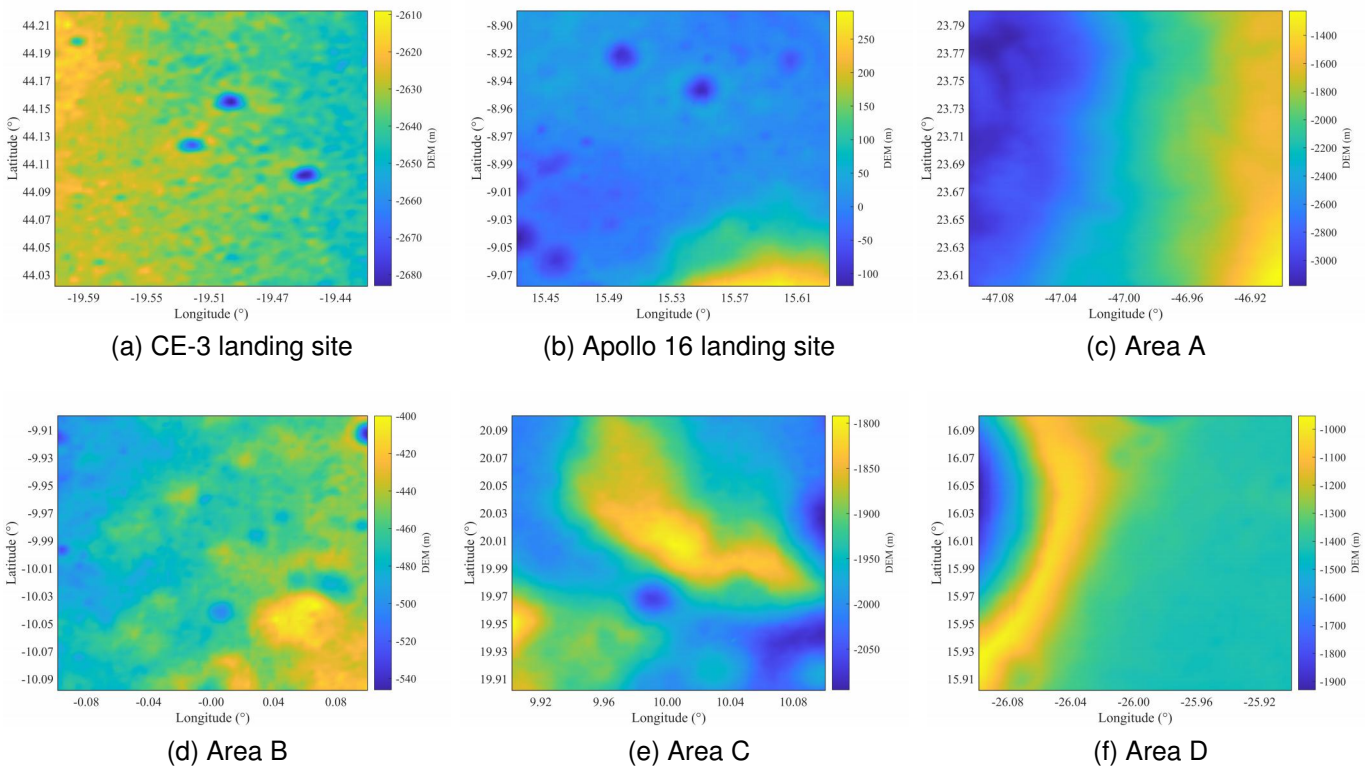

(a) CE-3 landing site (b) Apollo 16 landing site (c) Area A

(d) Area B (e) Area C (f) Area D

Fig. 10. Six regions on the lunar surface. The spatial resolution of the DEM in all regions is approximately 60 m.

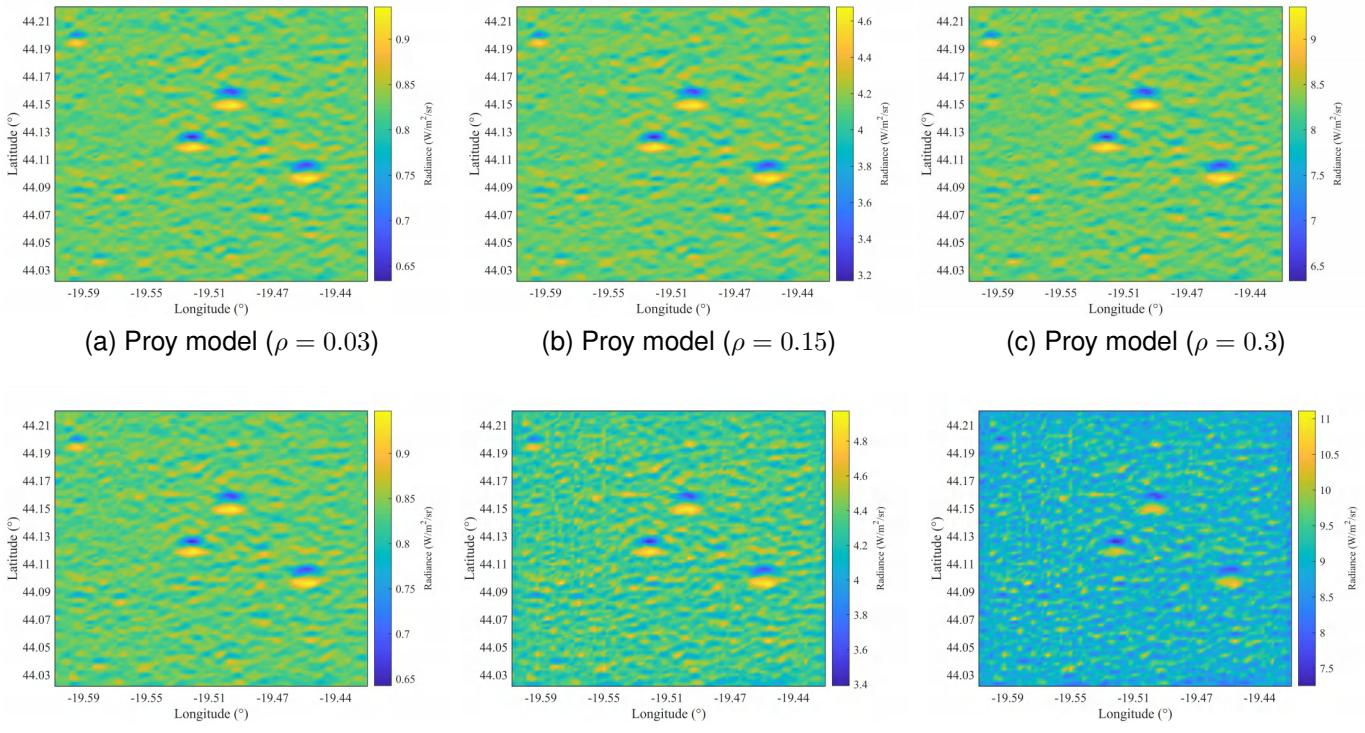

(a) Proy model ($\rho = 0.03$) (b) Proy model ($\rho = 0.15$) (c) Proy model ($\rho = 0.3$)

(d) MRRT model ($\rho = 0.03$) (e) MRRT model ($\rho = 0.15$) (f) MRRT model ($\rho = 0.3$)

Fig. 11. CE-3 landing site. Note that the "Proy model" refers to the result of the calculation term of the adjacent terrain irradiance in the Proy model, which is the result of a single reflection of radiation between terrains.

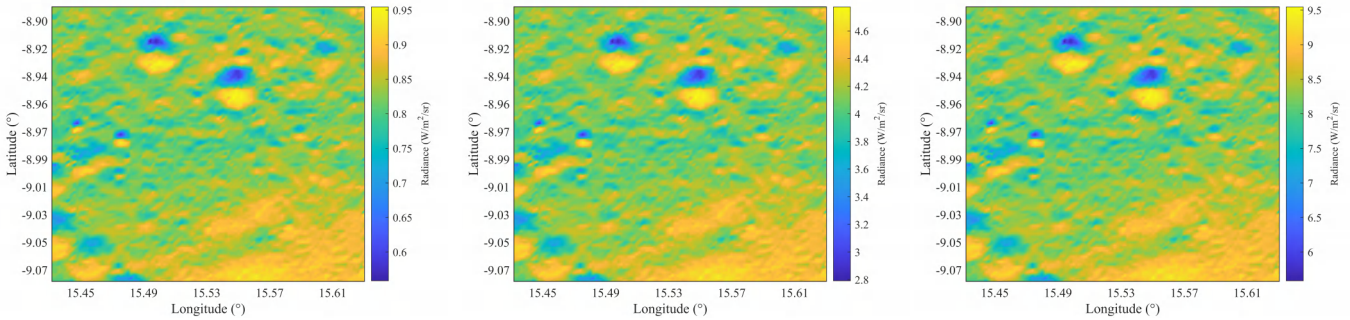

(a) Proy model ($\rho = 0.03$) (b) Proy model ($\rho = 0.15$) (c) Proy model ($\rho = 0.3$)

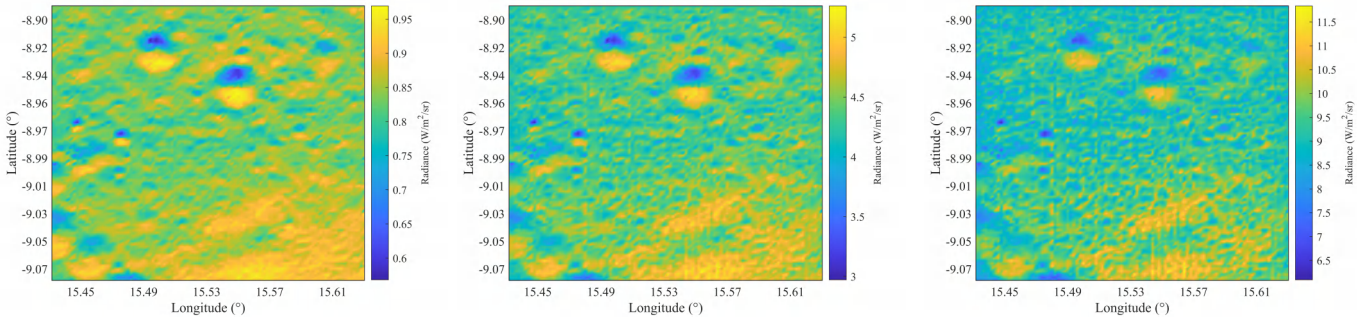

(d) MRRT model ($\rho = 0.03$) (e) MRRT model ($\rho = 0.15$) (f) MRRT model ($\rho = 0.3$)

Fig. 12. Apollo 16 landing site.

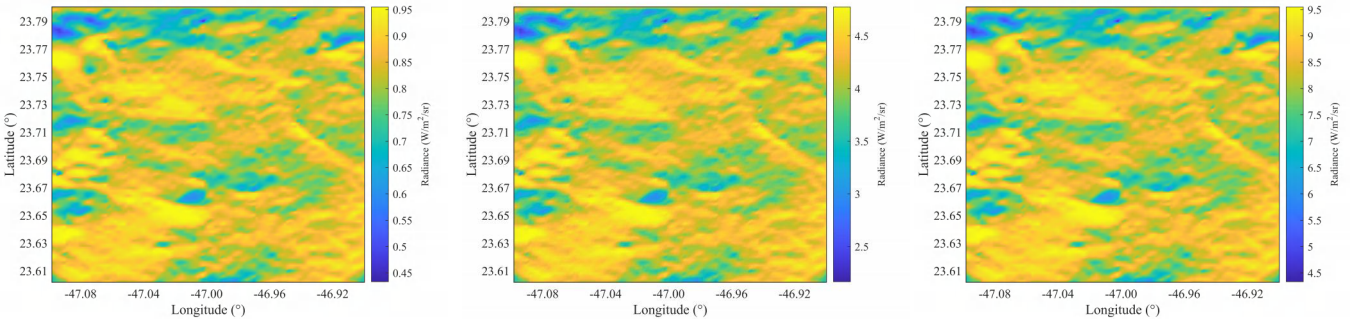

(a) Proy model ($\rho = 0.03$) (b) Proy model ($\rho = 0.15$) (c) Proy model ($\rho = 0.3$)

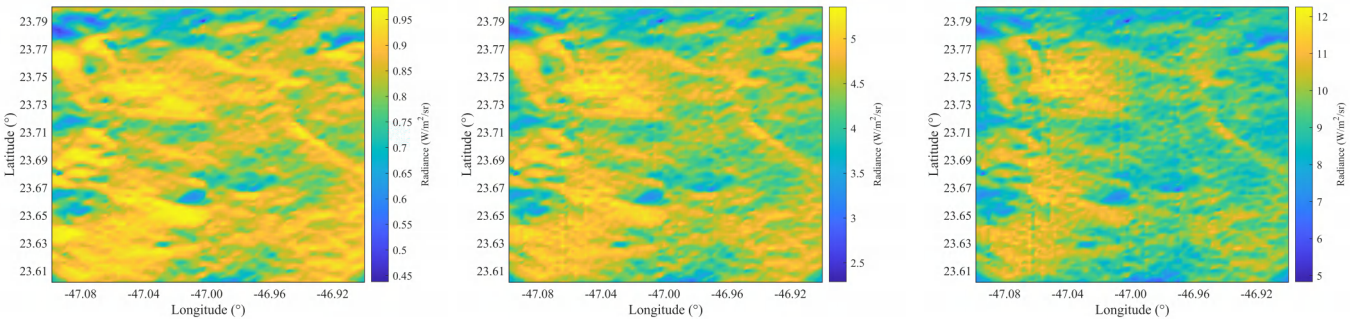

(d) MRRT model ($\rho = 0.03$) (e) MRRT model ($\rho = 0.15$) (f) MRRT model ($\rho = 0.3$)

Fig. 13. Area A.

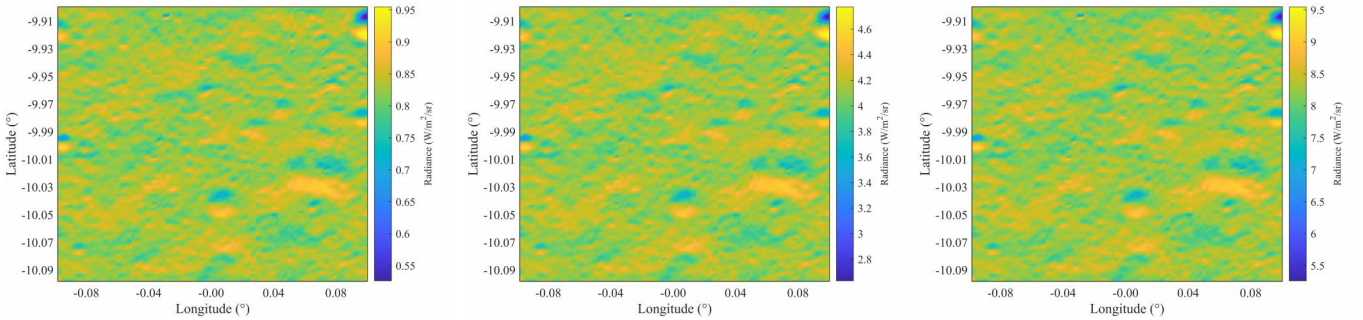

(a) Proy model ($\rho = 0.03$) (b) Proy model ($\rho = 0.15$) (c) Proy model ($\rho = 0.3$)

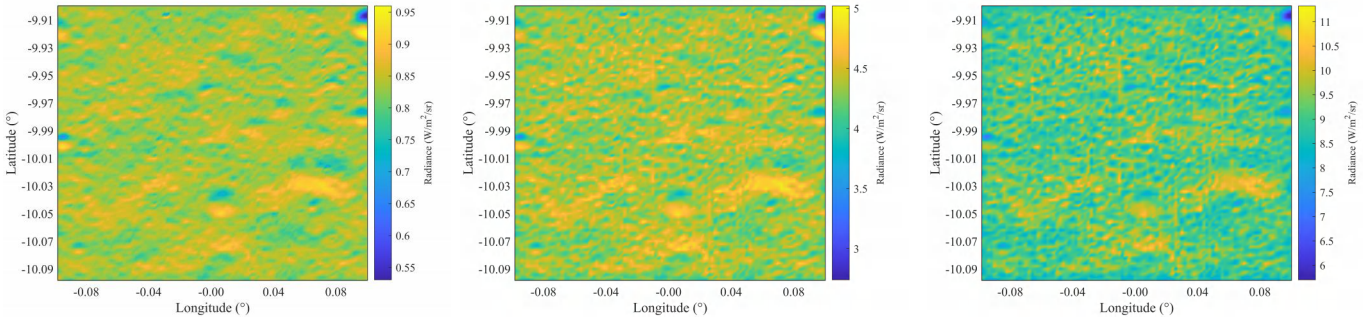

(d) MRRT model ($\rho = 0.03$) (e) MRRT model ($\rho = 0.15$) (f) MRRT model ($\rho = 0.3$)

Fig. 14. Area B.

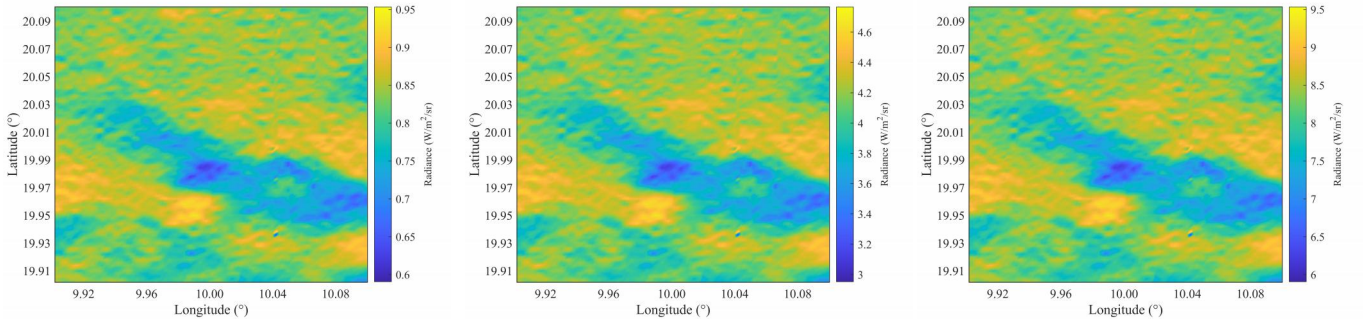

(a) Proy model ($\rho = 0.03$) (b) Proy model ($\rho = 0.15$) (c) Proy model ($\rho = 0.3$)

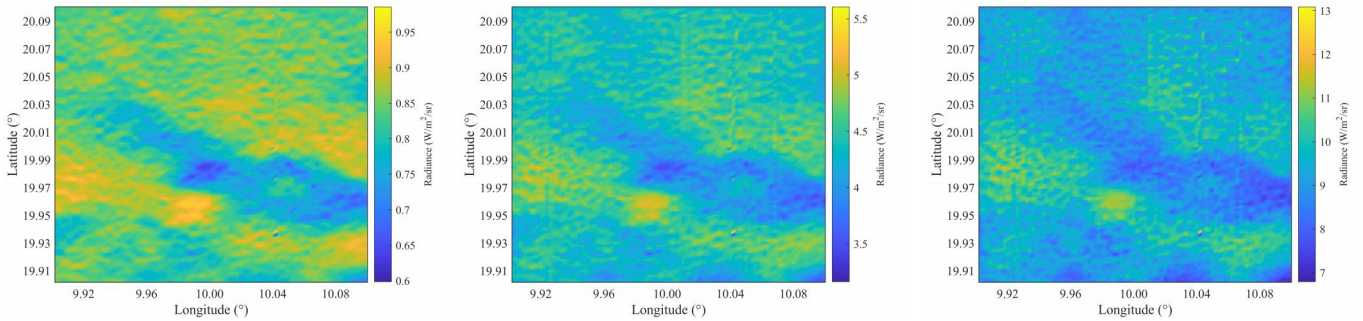

(d) MRRT model ($\rho = 0.03$) (e) MRRT model ($\rho = 0.15$) (f) MRRT model ($\rho = 0.3$)

Fig. 15. Area C.

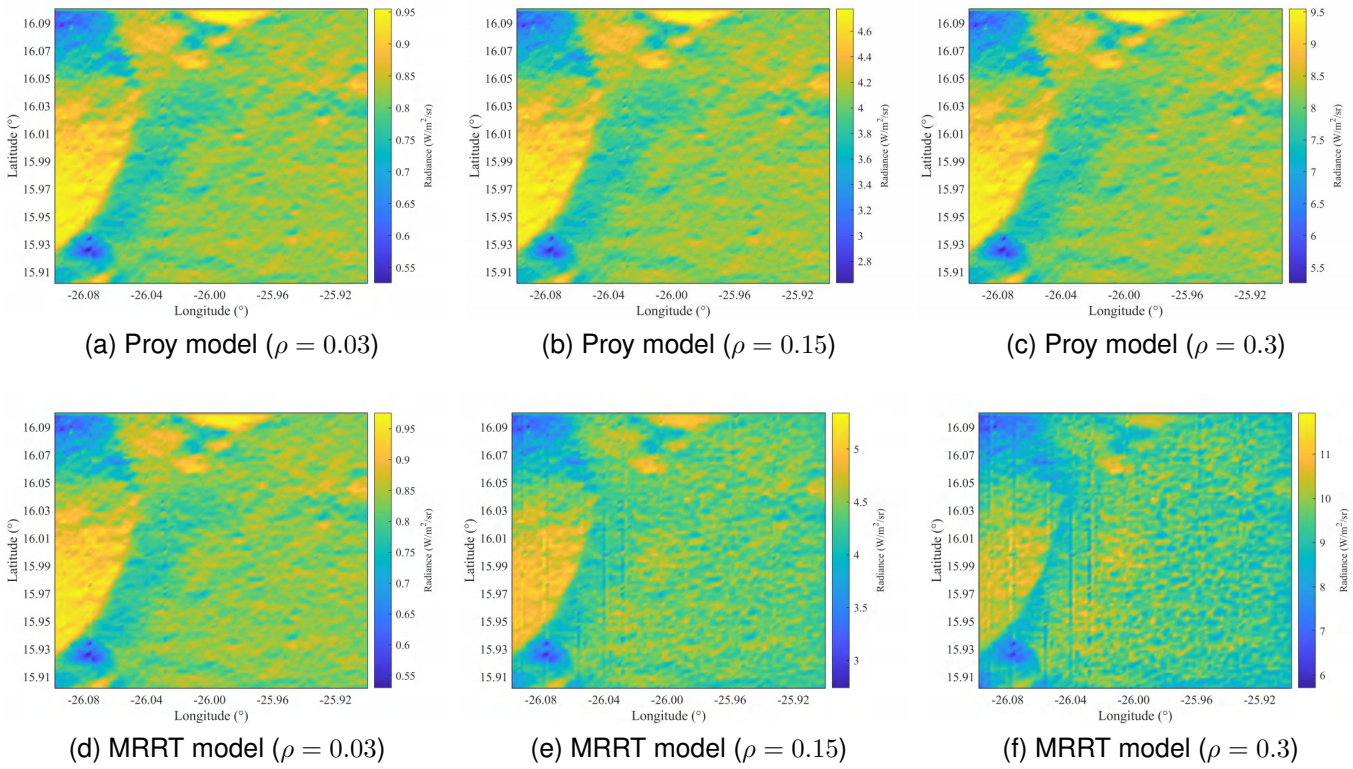

(a) Proy model ($\rho = 0.03$) (b) Proy model ($\rho = 0.15$) (c) Proy model ($\rho = 0.3$)

(d) MRRT model ($\rho = 0.03$) (e) MRRT model ($\rho = 0.15$) (f) MRRT model ($\rho = 0.3$)

Fig. 16. Area D.

TABLE II
INVERSION RESULTS OF MICROTOPOGRAPHY REFLECTANCE WITH THE SAME ILLUMINATION OBSERVATION GEOMETRY.

Area	Average slope (°)	Solar irradiance (W/m^2) 1	10	100	Standard deviation
CE3	1.92407516	0.143828	0.143799	0.143796	2.07E-05
Area B	2.89446438	0.142891	0.1429	0.142898	6.91E-06
Apollo16	5.04236565	0.140781	0.140801	0.140803	1.38E-05
Area C	5.73137887	0.141797	0.141826	0.141827	2.07E-05
Area D	10.1268984	0.142344	0.142363	0.142363	1.38E-05
Area A	17.146157	0.139883	0.139888	0.139886	3.45E-06

[1] The standard deviation of the retrieved reflectance for different solar incident irradiance is calculated.

reflectance; the order of magnitude of the inversion reflectance standard deviation for different solar incident irradiances is between 10^{-5} and 10^{-6}. However, under the same solar irradiance, the inversion reflectance of the microtopography of different areas has an obvious difference.

By sorting the results according to the average slope of the six areas, it can be found that the reflectance inversion results of the microtopography do not decline monotonically with increasing average slope. This is because, due to the relief of the terrain, different illumination observation geometries will cause a change in the reflected radiance in the observation direction, which is not necessarily monotonically increasing or decreasing. Therefore, if the multiple observed regions have the same illumination observation geometry and the same incident irradiance and observed radiance, the relationship between the reflectance inversion results and the topography is still unpredictable. This further demonstrates the importance of simulating multiple reflections of radiation between terrains to obtain the real terrain reflectance.

D. Inversion of microtopography reflectance by the IIM orbit data

The Chang'e-3 landing region and Apollo 16 landing region are taken as examples. We select IIM orbit data with numbers 2565, 2224, and 2843. Of these, IIM 2565 contains the Chang'e-3 landing site, and 2224 and 2843 contain the Apollo 16 landing site. The IIM orbit information is shown in Table III.

The in situ radiance and REFF (see Equation (B1)) of the Chang'e-3 landing site are taken as the standards to calculate the reflectance factor of the IIM orbit. The inversion target region uses the region shown in Fig. 10(a), which is 100×100 pixels in size and has a spatial resolution of approximately 60 m. The microarea reflectance retrieved by MRRT is the

TABLE III
IIM ORBITAL INFORMATION CORRESPONDING TO THE CE-3 AND APOLLO 16 LANDING SITES

Area	IIM orbit	Instrument Zenith Angle	Instrument Azimuth angle	Solar Zenith Angle	Solar Azimuth Angle	Phase Angle
CE3	2565	4.074523	91.10493	42.9412	178.1141	43.04256
Apollo16	2224	4.036909	271.5435	28.56248	290.5813	25.74082
	2843	4.071925	271.6117	26.92407	69.90193	28.53868

[1] Angles are in degrees.

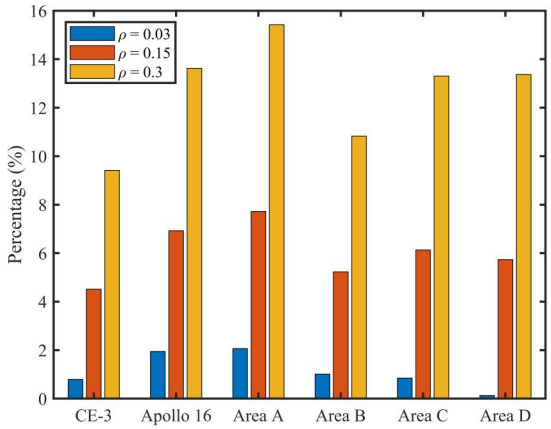

Fig. 17. Increased percentage of BRF for different target areas relative to the inner microtopography reflectance with the same illumination observation geometry. The reflectance ρ values of the microtopography inside the target regions are 0.03, 0.15, and 0.3.

slope surface reflectance constructed by DEM, which is the real terrain surface reflectance.

Fig. 18(a) shows that the REFF of the in situ measurements is almost "5" > "6" > "7" > "8", while the REFF of calibration with the in situ measurements is "7" > "6" > "5" > "8". Moreover, the REFF of the calibration and the REFF of the in situ measurements of the corresponding site are very different. The curves of "Calibration 5" and "Calibration 8" are located among the curves of "5", "6", "7", and "8". The inversion microtopography reflectance curve by the MRRT model is located above the curve "Calibration 5" and bottom of the curve "Calibration 6", and near the curve "5". For the same region, the reflectance curves should be similar. It can be found that the curves of "Calibration 5", "Calibration 8" and "MRRT" are consistent with this inference. Among them, the inversion results of the MRRT model are larger, which may be because the reflected radiance and reflectance measured in situ at the four stations represent fewer around areas, while the Chang'e-3 landing zone selected in this paper is slightly larger than the area observed at the four stations. Therefore, there may be other microareas with large reflectance inside the target region (i.e., the Chang'e-3 landing region selected in this paper), which leads to the large reflectance inversion results of the microtopography retrieved by the MRRT model.

In addition, both calibration and MRRT curves are calculated under the illumination observation geometry of IIM radiance data itself, while the illumination observation geometry of curve "5", "6", "7", and "8" is (30°, 0°, 30°), which may also be the reason why the calibration reflectance is quite different from the in-situ measurement reflectance. However, because the MRRT model in this paper assumes that the microarea surfaces are Lambertian, the MRRT curve can still be compared with the in situ measurement curves.

Fig. 18(b) shows that the calibration REFF results of IIM 2224 and 2843 are obviously two sets, in which the set of IIM 2843 is larger than IIM 2224 at each site. Some of the calibration curves are near the curves of 62231 reflectances. The inversion reflectance curves of IIM 2224 and 2843, which have different illumination observation geometry, are very close. This proves the accuracy of MRRT reflectance inversion to a certain extent. The difference between the two curves may be because MRRT assumes that the microregion is Lambertian, while the actual terrain situation is not Lambertian in a complete sense, so there are some differences in the inversion results. Although some calibration curves are close to the 62231 reflectance curve, while the MRRT inversion results are much smaller than the 62231 curves, studies have shown a difference in composition between the Apollo 16 landing site and the actual lunar soil sample 62231, with a reflectance spectrum nearly twice as large as that observed by remote-sensing sensors [14]. The inversion results of the MRRT in this paper also accord with this conclusion.

For Figs. 18(a) and (b), the trend of the reflectance of all curves is similar. The last band (the 31st band of IIM) reflectance at the calibration curve and MRRT curve is sharply reduced compared with the previous band. The 31st band of the IIM may also be inaccurate.

V. CONCLUSION

In this paper, a new model for quantifying multiple reflections of radiation between terrains (MRRT) is presented. Based on the adjacent terrain irradiance formula of the first-order reflection proposed by Proy, the second-order to the nth-order reflections of radiation between terrains are derived. According to formula (25), the MRRT model establishes the relationship between the BRF of the observed pixel and the true reflectance of the microterrain inside the observed pixel area, which shows that the terrain effect on the BRF mainly comes from the true reflectance of the terrain surface, the terrain undulation, the incident irradiance on the terrain surface and the masking in the observation direction.

The establishment of the new model is helpful to the study of regional radiation characteristics of the lunar surface and to select suitable lunar surface radiation calibration fields. Compared with the ROLO model based on modeling the integration of the radiance of the entire lunar surface, the

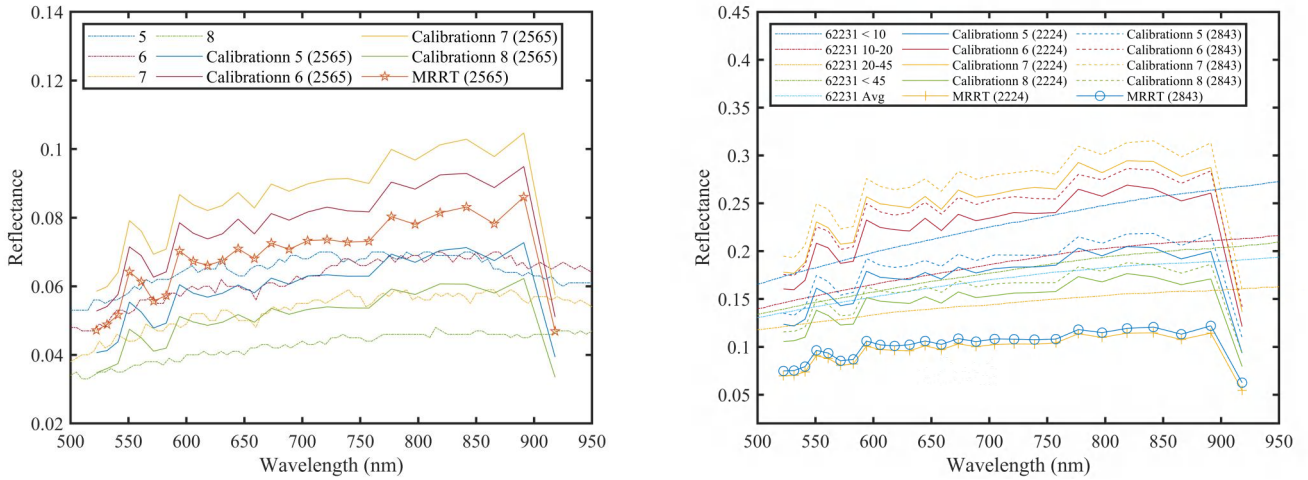

(a) Chang'e-3 landing site (b) Apollo 16 landing site

Fig. 18. Inversion reflectance spectra. Legend "Calibration 5" represents the reflectance factor calibration with in-situ measurements at site 5 of the Chang'e-3 landing site, and the legend "MRRT" represents the inversion microtopography reflectance by the MRRT model in this paper.

new model does not restrict the specific selection of the lunar surface region and is less affected by the different albedos of the lunar surface. Therefore, a region with a uniform material distribution, small albedo difference, and low topography undulation can be selected to establish the lunar surface radiometric calibration field with the advantage of providing stable radiation characteristics.

In this work, we demonstrate the importance of considering multiple reflections of radiation between terrains. The new model is applied to the lunar surface region and obtains clearer terrain details than the Proy model. Through the inversion of IIM orbit data, the reflectance curve of the Chang'e-3 landing area is similar to the reflectance measured in situ, and the reflectance curves of the Apollo16 landing area are almost consistent under different illumination observation geometries. This shows that the MRRT model can effectively eliminate the topographic effect.

The model presented in this paper can be used to retrieve the true reflectance of various topographic regions of the lunar surface. When using the model, it is recommended to apply it to an area with a high-resolution DEM. Generally, the higher the DEM accuracy is, the higher the accuracy of the modeling of multiple reflection processes. In addition, the MRRT model is recommended for use in combination with the Hapke model for retrieval of material in complex terrain areas; that is, the reflectance retrieved from the MRRT model is used as the true reflectance of the terrain.

Nevertheless, the model is still worth improving the accuracy of each quantity in Equations (16) to (25), such as the initial incident irradiance E_0 on the slope surface and the mutually visible radiation factor Γ between terrains. The research of this part can refer to the radiosity method of computer imaging, which has some similarities with the model in this paper. In addition, the application of the model to a larger scale of the lunar surface is still worthy of further study.

Our future work will focus on measuring the specific accuracy of the MRRT model in lunar calibration, such as comparison with the ROLO model, to more comprehensively evaluate the advantages of the proposed model in regional calibration.

ACKNOWLEDGMENT

We thank all the editors and reviewers for their enthusiasm and contributions to this article. They provided many valuable suggestions, which are of great help to the improvement of the content of this paper.

APPENDIX A
IMAGE ROTATION ERROR UNDER DIFFERENT INTERPOLATION METHODS

In this paper, the image is rotated to match the azimuth of the solar incident radiation, so that the relative azimuth of the image and the sun is 0°. Since the coordinates of the rotated image pixels are no longer integers, the values of the rotated pixels must be interpolated. Commonly used image interpolation methods are nearest neighbor interpolation, bilinear interpolation, and bicubic interpolation. Equations (A1) and (A2) are used to calculate the errors of the first-time rotation and second-time rotation (opposite to the direction of the first rotation) of the six groups of DEMs (see Fig. 10), respectively, and the results are shown in Table A1 and Table A2. Obviously, $error_1$ and $error_2$ are very small, among which the bicubic interpolation method has the smallest errors.

$$error_1 = \frac{\sum I_1 - \sum I}{\sum I} \times 100\% \tag{A1}$$

$$error_2 = \frac{\sum I_2^{'} - \sum I}{\sum I} \times 100\% \tag{A2}$$

where $\sum$ means the sum of all elevation values in the DEM. Each rotation of the image increases the size of the image.

TABLE A1
THE FIRST-TIME ROTATION ERROR OF THE IMAGE: $error_1$

Area	Method	Rotation angle (°)											
		30	60	90	120	150	180	210	240	270	300	330	360
CE3	nearest	9.61E-05	1.02E-04	-1.33E-16	9.52E-05	1.01E-04	0.00E+00	9.80E-05	1.02E-04	-1.33E-16	9.83E-05	1.01E-04	0.00E+00
	bilinear	-6.01E-06	-5.70E-06	-1.33E-16	-6.01E-06	-5.70E-06	0.00E+00	-6.01E-06	-5.70E-06	-1.33E-16	-6.01E-06	-5.70E-06	0.00E+00
	bicubic	2.57E-05	2.57E-05	-1.33E-16	2.57E-05	2.57E-05	0.00E+00	2.57E-05	2.57E-05	-1.33E-16	2.57E-05	2.57E-05	0.00E+00
Apollo16	nearest	-1.49E-03	-9.69E-05	-1.26E-16	-8.21E-04	1.06E-04	-1.26E-16	-1.27E-03	-8.31E-05	-1.26E-16	-1.35E-03	2.17E-04	0.00E+00
	bilinear	-4.20E-05	-2.42E-06	-1.26E-16	-4.20E-05	-2.42E-06	-1.26E-16	-4.20E-05	-2.42E-06	-1.26E-16	-4.20E-05	-2.42E-06	0.00E+00
	bicubic	7.38E-05	6.78E-05	-1.26E-16	7.38E-05	6.78E-05	-1.26E-16	7.38E-05	6.78E-05	-1.26E-16	7.38E-05	6.78E-05	0.00E+00
Area A	nearest	1.33E-04	5.97E-05	3.03E-16	8.01E-05	1.12E-04	0.00E+00	1.26E-04	6.34E-05	0.00E+00	1.33E-04	7.13E-05	0.00E+00
	bilinear	-4.97E-06	-6.03E-06	3.03E-16	-4.97E-06	-6.03E-06	0.00E+00	-4.97E-06	-6.03E-06	0.00E+00	-4.97E-06	-6.03E-06	0.00E+00
	bicubic	2.44E-05	2.45E-05	3.03E-16	2.44E-05	2.45E-05	0.00E+00	2.44E-05	2.45E-05	0.00E+00	2.44E-05	2.45E-05	0.00E+00
Area B	nearest	1.22E-04	6.22E-05	0.00E+00	1.18E-04	8.28E-05	-1.89E-16	1.14E-04	6.01E-05	1.89E-16	1.18E-04	7.38E-05	0.00E+00
	bilinear	-5.90E-06	-6.07E-06	0.00E+00	-5.90E-06	-6.07E-06	-1.89E-16	-5.90E-06	-6.07E-06	1.89E-16	-5.90E-06	-6.07E-06	0.00E+00
	bicubic	2.50E-05	2.57E-05	0.00E+00	2.50E-05	2.57E-05	-1.89E-16	2.50E-05	2.57E-05	1.89E-16	2.50E-05	2.57E-05	0.00E+00
Area C	nearest	8.91E-05	9.90E-05	1.80E-16	9.29E-05	1.01E-04	-3.60E-16	1.04E-04	9.95E-05	1.80E-16	1.03E-04	9.88E-05	0.00E+00
	bilinear	-5.87E-06	-5.63E-06	1.80E-16	-5.87E-06	-5.63E-06	-3.60E-16	-5.87E-06	-5.63E-06	1.80E-16	-5.87E-06	-5.63E-06	0.00E+00
	bicubic	2.61E-05	2.63E-05	1.80E-16	2.61E-05	2.63E-05	-3.60E-16	2.61E-05	2.63E-05	1.80E-16	2.61E-05	2.63E-05	0.00E+00
Area D	nearest	1.30E-04	9.52E-05	1.30E-16	1.49E-04	6.89E-05	2.60E-16	1.38E-04	8.75E-05	2.60E-16	1.36E-04	8.89E-05	0.00E+00
	bilinear	-5.99E-06	-6.76E-06	1.30E-16	-5.99E-06	-6.76E-06	2.60E-16	-5.99E-06	-6.76E-06	2.60E-16	-5.99E-06	-6.76E-06	0.00E+00
	bicubic	2.63E-05	2.61E-05	1.30E-16	2.63E-05	2.61E-05	2.60E-16	2.63E-05	2.61E-05	2.60E-16	2.63E-05	2.61E-05	0.00E+00

TABLE A2
THE SECOND-TIME ROTATION ERROR OF THE IMAGE: $error_2$

Area	Method	Rotation angle (°)											
		30	60	90	120	150	180	210	240	270	300	330	360
CE3	nearest	-3.60E-03	-3.60E-03	0.00E+00	-3.60E-03	-3.60E-03	0.00E+00	-3.60E-03	-3.60E-03	0.00E+00	-3.60E-03	-3.60E-03	0.00E+00
	bilinear	-6.65E-03	-6.65E-03	0.00E+00	-6.65E-03	-6.65E-03	0.00E+00	-6.65E-03	-6.65E-03	0.00E+00	-6.65E-03	-6.65E-03	0.00E+00
	bicubic	-1.87E-03	-1.87E-03	0.00E+00	-1.87E-03	-1.87E-03	0.00E+00	-1.87E-03	-1.87E-03	0.00E+00	-1.87E-03	-1.87E-03	0.00E+00
Apollo16	nearest	-8.70E-03	-7.36E-03	0.00E+00	-8.13E-03	-7.27E-03	0.00E+00	-8.32E-03	-7.36E-03	0.00E+00	-8.50E-03	-7.09E-03	0.00E+00
	bilinear	-1.27E-02	-1.26E-02	0.00E+00	-1.27E-02	-1.26E-02	0.00E+00	-1.27E-02	-1.26E-02	0.00E+00	-1.27E-02	-1.26E-02	0.00E+00
	bicubic	-3.66E-03	-3.64E-03	0.00E+00	-3.66E-03	-3.64E-03	0.00E+00	-3.66E-03	-3.64E-03	0.00E+00	-3.66E-03	-3.64E-03	0.00E+00
Area A	nearest	-3.47E-03	-3.52E-03	0.00E+00	-3.51E-03	-3.48E-03	0.00E+00	-3.48E-03	-3.52E-03	0.00E+00	-3.47E-03	-3.51E-03	0.00E+00
	bilinear	-6.51E-03	-6.52E-03	0.00E+00	-6.51E-03	-6.52E-03	0.00E+00	-6.51E-03	-6.52E-03	0.00E+00	-6.51E-03	-6.52E-03	0.00E+00
	bicubic	-1.83E-03	-1.83E-03	0.00E+00	-1.83E-03	-1.83E-03	0.00E+00	-1.83E-03	-1.83E-03	0.00E+00	-1.83E-03	-1.83E-03	0.00E+00
Area B	nearest	-3.60E-03	-3.65E-03	0.00E+00	-3.60E-03	-3.63E-03	0.00E+00	-3.60E-03	-3.66E-03	0.00E+00	-3.61E-03	-3.64E-03	0.00E+00
	bilinear	-6.69E-03	-6.69E-03	0.00E+00	-6.69E-03	-6.69E-03	0.00E+00	-6.69E-03	-6.69E-03	0.00E+00	-6.69E-03	-6.69E-03	0.00E+00
	bicubic	-1.88E-03	-1.88E-03	0.00E+00	-1.88E-03	-1.88E-03	0.00E+00	-1.88E-03	-1.88E-03	0.00E+00	-1.88E-03	-1.88E-03	0.00E+00
Area C	nearest	-3.67E-03	-3.66E-03	0.00E+00	-3.66E-03	-3.66E-03	0.00E+00	-3.65E-03	-3.66E-03	0.00E+00	-3.65E-03	-3.67E-03	0.00E+00
	bilinear	-6.77E-03	-6.77E-03	0.00E+00	-6.77E-03	-6.77E-03	0.00E+00	-6.77E-03	-6.77E-03	0.00E+00	-6.77E-03	-6.77E-03	0.00E+00
	bicubic	-1.91E-03	-1.91E-03	0.00E+00	-1.91E-03	-1.91E-03	0.00E+00	-1.91E-03	-1.91E-03	0.00E+00	-1.91E-03	-1.91E-03	0.00E+00
Area D	nearest	-3.76E-03	-3.82E-03	0.00E+00	-3.74E-03	-3.84E-03	0.00E+00	-3.75E-03	-3.82E-03	0.00E+00	-3.75E-03	-3.82E-03	0.00E+00
	bilinear	-7.00E-03	-7.00E-03	0.00E+00	-7.00E-03	-7.00E-03	0.00E+00	-7.00E-03	-7.00E-03	0.00E+00	-7.00E-03	-7.00E-03	0.00E+00
	bicubic	-1.97E-03	-1.97E-03	0.00E+00	-1.97E-03	-1.97E-03	0.00E+00	-1.97E-03	-1.97E-03	0.00E+00	-1.97E-03	-1.97E-03	0.00E+00

Therefore, I, I_1, and $I_2^{'}$ are the original DEM, the DEM after the first-time rotation and the DEM cropped to the original DEM size after the second rotation. We align the center of the original image I and the second-time rotated image I_2 and then intercept the corresponding region according to the size of I, denoted as $I_2^{'}$.

APPENDIX B
DEFINITION OF REFLECTANCE USED IN THIS PAPER

1. Reflectance Factor (REFF): The ratio of the radiance reflected from the surface into a given direction to that of a standard panel and corrected with the REFF of the standard panel at the measurement geometry. The equation is [38]:

$$REFF(\lambda,\theta_0,\phi_0,\theta_v,\varphi_v) = \frac{I_{sample}(\lambda,\theta_0,\phi_0,\theta_v,\varphi_v)}{I_{std}(\lambda,\theta_0,\phi_0,\theta_v,\varphi_v)} \times R_{std}(\lambda,\theta_0,\phi_0,\theta_v,\varphi_v) \quad \text{(B1)}$$

where λ, θ_0, ϕ_0, θ_v, and φ_v are the wavelength, Sun zenith angle, Sun azimuth angle, view zenith angle, and view azimuth angle, respectively. I_{sample} is the radiance of the target measured by the instrument, I_{std} is the radiance of the diffuser panel measured by the instrument, and R_{std} is the REFF of the diffuser panel.

2. Bidirectional Reflectance Factor (BRF): The ratio of the radiance reflected from the surface into a given direction to that of a perfectly diffuse surface under the same illumination observation geometry. The equation is:

$$BRF(\lambda,\theta_0,\phi_0,\theta_v,\varphi_v) = \frac{\pi \cdot L_v(\lambda,\theta_0,\phi_0,\theta_v,\varphi_v) \cdot D^2}{J(\lambda) \cdot cos(\theta_0)} \quad \text{(B2)}$$

where λ, θ_0, ϕ_0, θ_v, and φ_v are the wavelength, Sun zenith angle, Sun azimuth angle, view zenith angle, and view azimuth angle, respectively. L_v is the radiance measured by the instrument, and J is the solar irradiance at the surface of the IIM, which is calculated by Equation (26). D is the Sun-Moon distance in kilometers at the observation time divided by the standard Sun-Moon distance (149,597,870 km). In this study, the value of D is 1.

REFERENCES

[1] C. M. Pieters, "The Moon as a spectral calibration standard enabled by lunar samples: The Clementine example," *Workshop on New Views of the Moon 2*, 1999.

[2] H. H. Kieffer, "Photometric stability of the lunar surface," *Icarus*, vol. 130, no. 2, pp. 323–327, 1997.

[3] T. Stone and H. Kieffer, "Absolute Irradiance of the Moon for On-orbit Calibration," *Proceedings of SPIE - The International Society for Optical Engineering*, vol. 4814, 2002.

[4] T. C. Stone and H. H. Kieffer, "Assessment of uncertainty in rolo lunar irradiance for on-orbit calibration," in *Conference on Earth Observing Systems IX; 20040802,4-6; Denver,CO(US)*, 2004.

[5] L. Zhang, P. Zhang, X. Hu, L. Chen, and M. Min, "A novel hyperspectral lunar irradiance model based on ROLO and mean equigonal albedo," *Optik*, vol. 142, pp. 657–664, 2017,8.

[6] J. Sun and X. Xiong, "Improved Lunar Irradiance Model Using Multiyear MODIS Lunar Observations," *IEEE Transactions on Geoscience and Remote Sensing*, vol. 59, no. 6, pp. 5154–5170, 2021,6.

[7] Z. Ouyang, *Introduction to Lunar Science*. China Aerospace Publishing House, 2005.

[8] R. Jaumann, H. Hiesinger, M. Anand, I. A. Crawford, R. Wagner, F. Sohl, B. L. Jolliff, F. Scholten, M. Knapmeyer, H. Hoffmann, H. Hussmann, M. Grott, S. Hempel, U. Köhler, K. Krohn, N. Schmitz, J. Carpenter, M. Wieczorek, T. Spohn, M. S. Robinson, and J. Oberst, "Geology, geochemistry, and geophysics of the Moon: Status of current understanding," *Planetary and Space Science*, vol. 74, no. 1, pp. 15–41, 2012,12.

[9] Y. Z. Cai and W. Z. Fa, "Meter-Scale Topographic Roughness of the Moon: The Effect of Small Impact Craters," *Journal of Geophysical Research: Planets*, vol. 125, no. 8, p. 24, 2020,8.

[10] J. D. Goguen, T. C. Stone, H. H. Kieffer, and B. J. Buratti, "A new look at photometry of the Moon," *Icarus*, vol. 208, no. 2, pp. 548–557, 2010,8.

[11] C. Schaaf, X. Li, and A. Strahler, "Topographic effects on bidirectional and hemispherical reflectances calculated with a geometric-optical canopy model," *IEEE Transactions on Geoscience and Remote Sensing*, vol. 32, no. 6, pp. 1186–1193, 1994.

[12] J. Wen, X. Zhao, Q. Liu, Y. Tang, and B. Dou, "An Improved Land-Surface Albedo Algorithm With DEM in Rugged Terrain," *IEEE Geoscience and Remote Sensing Letters*, vol. 11, no. 4, pp. 883–887, 2014,4.

[13] J. Wen, Q. Liu, Q. Xiao, Q. Liu, D. You, D. Hao, S. Wu, and X. Lin, "Characterizing Land Surface Anisotropic Reflectance over Rugged Terrain: A Review of Concepts and Recent Developments," *Remote Sensing*, vol. 10, no. 3, p. 370, 2018.

[14] Y. Wu, X. Hu, and S. Li, "The Irradiance Model of the Moon and Its Implication on the On-orbit Calibration of Spacecraft," in *The 4th Annual Conference on High Resolution Earth Observation*, 2017, p. 9.

[15] J. Zhang, Z. Ling, W. Zhang, X. Ren, C. Li, and J. Liu, "Photometric modeling of the Moon using Lommel-Seeliger function and Chang'E-1 IIM data," *Chinese Science Bulletin*, vol. 58, no. 36, pp. 4588–4592, 2013.

[16] S. B. Chen, J. R. Wang, P. J. Guo, and M. C. Wang, "Sandmeier Model Based Topographic Correction to Lunar Spectral Profiler (SP) Data from KAGUYA Satellite," *Spectroscopy and Spectral Analysis*, vol. 34, no. 9, pp. 2573–2577, 2014.

[17] X. Xu, J. Liu, D. Liu, B. Liu, and R. Shu, "Photometric Correction of Chang'E-1 Interference Imaging Spectrometer's (IIM) Limited Observing Geometries Data with Hapke Model," *Remote Sensing*, vol. 12, no. 22, p. 3676, 2020.

[18] X. Lin, J. Wen, S. Wu, D. Hao, Q. Xiao, and Q. Liu, "Advances in topographic correction methods for optical remote sensing imageries," *Journal of Remote Sensing*, vol. 24, no. 8, pp. 958–974, 2020.

[19] S. Soenen, D. Peddle, and C. Coburn, "SCS+C: A modified Sun-canopy-sensor topographic correction in forested terrain," *IEEE Transactions on Geoscience and Remote Sensing*, vol. 43, no. 9, pp. 2148–2159, 2005,9.

[20] B. Hapke, "An Improved Theoretical Lunar Photometric Function." *The Astronomical Journal*, vol. 71, no. 5, p. 386, 1966.

[21] B. Hapke, "Bidirectional reflectance spectroscopy: 1. Theory," *Journal of Geophysical Research: Solid Earth*, vol. 86, no. B4, pp. 3039–3054, 1981,4,10.

[22] B. Hapke, *Theory of Reflectance and Emittance Spectroscopy*, 2nd ed. New York: United States of America by Cambridge University Press, 2012, vol. 47.

[23] B. W. Hapke, "A theoretical photometric function for the lunar surface," *Journal of Geophysical Research*, vol. 68, no. 15, pp. 4571–4586, 1963,8,1.

[24] B. Zunjian, Q. Jianbo, W. Shengbiao, W. Yusheng, L. Shouyang, X. Baodong, D. Yongming, C. Biao, L. Hua, H. Huaguo, X. Qing, and L. Qinhuo, "A review on the development and application of three dimensional computer simulation mode of optical remote sensing," *Journal of Remote Sensing*, vol. 25, no. 2, pp. 559–576, 2021.

[25] K. Muinonen, H. Parviainen, J. Näränen, J.-L. Josset, S. Beauvivre, P. Pinet, S. Chevrel, D. Koschny, B. Grieger, and B. Foing, "Lunar mare single-scattering, porosity, and surface-roughness properties with SMART-1 AMIE," *Astronomy & Astrophysics*, vol. 531, p. A150, 2011.

[26] U.-H. Wong, Y. Wu, H.-C. Wong, Y. Liang, and Z. Tang, "Modeling the Reflectance of the Lunar Regolith by a New Method Combining Monte Carlo Ray Tracing and Hapke's Model with Application to Chang'E-1 IIM Data," *The Scientific World Journal*, vol. 2014, pp. 1–14, 2014.

[27] C. PROY, D. TANRE, and P. DESCHAMPS, "Evaluation of topographic effects in remotely sensed data73," *Remote Sensing of Environment*, vol. 30, no. 1, pp. 21–32, 1989.

[28] S. Sandmeier and K. I. J. G. Itten, "A physically-based model to correct atmospheric and illumination effects in optical satellite data of rugged terrain," *IEEE Transactions on Geoscience and Remote Sensing*, vol. 35, no. 3, pp. 708–717, 1997.

[29] J. Dozier and J. Frew, "Rapid calculation of terrain parameters for radiation modeling from digital elevation data," *IEEE Transactions on Geoscience and Remote Sensing*, vol. 28, no. 5, pp. 963–969, 1990.

[30] H. Li, L. Xu, H. Shen, and L. Zhang, "A general variational framework considering cast shadows for the topographic correction of remote sensing imagery," *ISPRS Journal of Photogrammetry and Remote Sensing*, vol. 117, pp. 161–171, 2016,7.

[31] J. Wen, Q. Liu, Y. Tang, B. Dou, D. You, Q. Xiao, Q. Liu, and X. Li, "Modeling Land Surface Reflectance Coupled BRDF for HJ-1/CCD Data of Rugged Terrain in Heihe River Basin, China," *IEEE Journal of Selected Topics in Applied Earth Observations and Remote Sensing*, vol. 8, no. 4, pp. 1506–1518, 2015,4.

[32] J. Dozier, J. Bruno, and P. Downey, "A faster solution to the horizon problem," *Computers & Geosciences*, vol. 7, no. 2, pp. 145–151, 1981,1.

[33] R. Keys, "Cubic convolution interpolation for digital image processing," *IEEE Transactions on Acoustics, Speech, and Signal Processing*, vol. 29, no. 6, pp. 1153–1160, 1981.

[34] D. E. Smith, M. T. Zuber, G. A. Neumann, F. G. Lemoine, E. Mazarico, M. H. Torrence, J. F. McGarry, D. D. Rowlands, J. W. Head, T. H. Duxbury, O. Aharonson, P. G. Lucey, M. S. Robinson, O. S. Barnouin, J. F. Cavanaugh, X. Sun, P. Liiva, D.-d. Mao, J. C. Smith, and A. E. Bartels, "Initial observations from the Lunar Orbiter Laser Altimeter (LOLA)," *Geophysical Research Letters*, vol. 37, no. 18, pp. n/a–n/a, 2010.

[35] P. G. Lucey, G. A. Neumann, M. A. Riner, E. Mazarico, D. E. Smith, M. T. Zuber, D. A. Paige, D. B. Bussey, J. T. Cahill, A. McGovern, P. Isaacson, L. M. Corley, M. H. Torrence, H. J. Melosh, J. W. Head, and E. Song, "The global albedo of the Moon at 1064 nm from LOLA," *Journal of Geophysical Research: Planets*, vol. 119, no. 7, pp. 1665–1679, 2014.

[36] M. Barker, E. Mazarico, G. Neumann, M. Zuber, J. Haruyama, and D. Smith, "A new lunar digital elevation model from the Lunar Orbiter Laser Altimeter and SELENE Terrain Camera," *Icarus*, vol. 273, pp. 346–355, 2016.

[37] F.-F. Wang, J.-J. Liu, C.-L. Li, X. Ren, L.-L. Mu, W. Yan, W.-R. Wang, J.-T. Xiao, X. Tan, X.-X. Zhang, X.-D. Zou, and X.-Y. Gao, "A new lunar absolute control point: Established by images from the landing camera on Change-3," *Research in Astronomy and Astrophysics*, vol. 14, no. 12, pp. 1543–1556, 2014.

[38] Y. Wu, Z. Wang, W. Cai, and Y. Lu, "The Absolute Reflectance and New Calibration Site of the Moon," *The Astronomical Journal*, vol. 155, no. 5, p. 213, 2018.

[39] Z. He, R. Xu, C. Li, G. Lv, L. Yuan, B. Wang, R. Shu, and J. Wang, "Visible and near-infrared imaging spectrometer (VNIS) for in-situ lunar surface measurements," in *SPIE Proceedings*, vol. 9639. SPIE, 2015, pp. 498–509.

[40] Z. Ouyang, C. Li, Y. Zou, H. Zhang, C. Lü, J. Liu, J. Liu, W. Zuo, Y. Su, W. Wen, W. Bian, B. Zhao, J. Wang, J. Yang, J. Chang, H. Wang, X. Zhang, S. Wang, M. Wang, X. Ren, L. Mu, D. Kong, X. Wang, F. Wang, L. Geng, Z. Zhang, L. Zheng, X. Zhu, Y. Zheng, J. Li, X. Zou, C. Xu, S. Shi, Y. Gao, and G. Gao, "Primary scientific results of Chang'E-1 lunar mission," *Science China Earth Sciences*, vol. 53, no. 11, pp. 1565–1581, 2010.

[41] C. A. Gueymard, "The sun's total and spectral irradiance for solar energy applications and solar radiation models," *Solar Energy*, vol. 76, pp. 423–453, 2004.